Available online at www.sciencedirect.com

ScienceDirect

Geochimica et Cosmochimica Acta 293 (2021) 477–506

Geochimica et Cosmochimica Acta

www.elsevier.com/locate/gca

Silica-rich spinel harzburgite residues formed by fractional hybridization-melting of the intra-oceanic supra-subduction zone mantle: New evidence from TUBAF seamount peridotites

A. Bénard [a,*], O. Müntener [a], S. Pilet [a], R.J. Arculus [b], O. Nebel [c]

[a] Institute of Earth Sciences, University of Lausanne, 1015 Lausanne, Switzerland
[b] Research School of Earth Sciences, The Australian National University, 2601 Acton, ACT, Australia
[c] School of Earth, Atmosphere and Environment, Monash University, 3800 Clayton, VIC, Australia

Received 6 May 2020; accepted in revised form 2 November 2020; Available online 7 November 2020

Abstract

Recent studies of serpentine-free, spinel peridotite xenoliths from the mantle lithosphere beneath the active Kamchatka and West Bismarck arcs have shown that these rocks are enriched in silica and highly depleted in incompatible elements in comparison with melting residues of either primitive or mid-ocean ridge mantle. It has been suggested that the silica-rich nature of peridotites from the intra-oceanic, fore- and sub-arc mantle lithosphere, collectively referred to as 'Supra-Subduction Zone (SSZ) peridotites', is primarily of residual origin and inherited from source processes during partial melting in the SSZ mantle asthenosphere (mantle wedge). However, quantifying the contribution of post-melting processes to the silica-rich nature of SSZ peridotites has remained challenging.

Here we report petrological and major and trace element data for a new suite of spinel harzburgite xenoliths from the mantle lithosphere beneath TUBAF seamount, located in the fore-arc region of New Ireland (Papua New Guinea area). All samples are fresh peridotites displaying coarse-grained protogranular textures, and sometimes high orthopyroxene (up to ~29 wt %) at low clinopyroxene (≤4 wt%) contents, which are typical for SSZ peridotites worldwide. TUBAF peridotites in this study have suffered very little post-melting metasomatism through the formation of ≤1 wt% amphibole, which subsequently experienced decompression-induced breakdown during the xenolith ascent. Otherwise, the rocks display a high degree of inter-mineral equilibration and melting signatures preserved through sub-solidus re-equilibration. The bulk-rock chemistry of TUBAF peridotites record a Fe-Al correlation along the 25–30% melting isopleths from ~2 to <1 GPa, in combination with the distinctive enrichment in silica and (TiO_2, Al_2O_3, Na_2O)-depletion of SSZ peridotites. This strongly supports the melting origin of these 'residual SSZ signatures'. Bulk-rock and mineral lithophile trace element compositions of TUBAF xenoliths are similar to those of other residual SSZ peridotites, consistent with 25–30% of nearly-pure fractional melt extraction (critical mass porosity <0.001%) in the presence of a fluxing agent enriched in highly incompatible elements.

We re-assess earlier interpretations of the origins of TUBAF peridotites by melting at mid-ocean ridges. Instead, we show that these rocks have experienced their last melting event in the mantle wedge, similar to samples from the Izu-Bonin-Mariana fore-arc and the Kamchatka and West Bismarck arcs. We also demonstrate that post-melting metasomatism (including fibrous orthopyroxene that are absent from the samples in this study) is unrelated to the residual SSZ mantle signatures, for which we present the results of polybaric and isothermal flux-melting models including minor element partitioning parameterizations. These models imply that residual SSZ signatures form when previously depleted mantle protoliths are hybridized

* Corresponding author.
E-mail address: antoine.benard@unil.ch (A. Bénard).

https://doi.org/10.1016/j.gca.2020.11.001

by hydrous, silica-rich liquids. From the unique Fe-Al correlation in TUBAF peridotites and their low temperatures of equilibration, it appears that fractional hybridization-melting processes forming these rocks occurred in a fore-arc environment with shallow mantle decompression, likely during Oligocene to Miocene subduction along the Manus-Kilinailau trench.

Keywords: Silica enrichment; Peridotite; Subduction; Mantle wedge; Hybridization; Partial melting; Xenolith

1. INTRODUCTION

Lithospheric mantle peridotites found as xenoliths or dredged in intra-oceanic subduction zone systems, i.e. including fore-arc and sub−arc settings-collectively referred to as 'Supra-Subduction Zone (SSZ) peridotites' – are extremely rare. Only about twenty localities, mostly from the Western Pacific, have been studied, with a limited number of samples analyzed for their bulk-rock major element compositions (e.g. Maury et al., 1992; Parkinson and Pearce, 1998; McInnes et al., 2001; Ishimaru et al., 2007). Major element compositions are critical to decipher the petrogenesis of mantle peridotites, for instance in comparison with minor and trace elements, which are much more easily reset by post-melting modification processes (e.g. metasomatism in the mantle lithosphere; Ionov et al., 2002; Bénard and Ionov, 2012).

Petrological studies of SSZ peridotites have outlined the predominance of spinel harzburgite and dunite forming the mantle lithosphere in these areas (Maury et al., 1992; Parkinson and Pearce, 1998; McInnes et al., 2001; Ishimaru et al., 2007; Ionov, 2010; Ionov et al., 2013; Bénard et al., 2016, 2017a). Regarding major element compositions, the silica-rich nature of SSZ peridotites was first recognized and investigated by Herzberg (2004). In this seminal study, Herzberg stated that SSZ peridotites are generally 'too enriched in SiO_2 and too depleted in Al_2O_3 to be melting residues'. However, this conclusion was based on a comparison of SSZ peridotites with melting trends derived from the fertile KR-4003 lherzolite (Walter, 1998), which can only be considered as representative of the primitive mantle (PM) or the depleted mid-ocean ridge basalt mantle (DMM) reservoirs. As such, the effects of variable mantle source compositions on those of residues were not investigated.

Since Herzberg (2004), two studies have reported high-precision bulk-rock data for the analysis of fresh, orthopyroxene- and silica-rich SSZ peridotites from the Kamchatka (Avacha volcano; Ionov, 2010) and West Bismarck (Ritter volcano; Bénard et al., 2017a) arcs. These SSZ peridotites display strikingly similar and well-defined petrological features (coarse-grained, clinopyroxene-poor spinel harzburgite and dunite) and major element compositions (Bénard et al., 2017a). The silica-rich nature is common to both fore- and sub-arc mantle peridotites, with the former type best represented by the Izu-Bonin-Mariana (IBM) sample suite studied by Parkinson and Pearce (1998). Based on melting models, Bénard et al. (2017a) further suggested that the silica-rich nature of all these mantle peridotites was inherited from the last partial melting (simply referred to as 'melting' hereafter) event in the SSZ mantle asthenosphere (mantle wedge) and not a result of post-melting metasomatic reactions.

Further insights on the nature of silica enrichment in SSZ peridotites could be gained from high-pressure melting experiments, which predict various Fe-Al correlations in bulk rocks depending on whether melting is isobaric or polybaric (Herzberg, 2004). However, these trends are extremely rare in mantle peridotites; they can be easily reset by post-melting processes, as Fe enrichment is common during metasomatism in the mantle lithosphere (e.g. Ionov et al., 2005). In fact, Fe-Al correlations have been reported in only three residual mantle peridotite suites worldwide, which include the Horoman massif (Japan; Takazawa et al., 1996, 2000), and xenoliths in continental, off-craton (Mongolia; Ionov, 2004, 2007; Ionov and Hofmann, 2007) and cratonic (Siberia; Doucet et al., 2012) settings. This feature is possibly present in samples from other localities but unrecognized in the original publications, such as is the case for a suite of abyssal peridotites (Mid-Atlantic Ridge; Stephens, 1997).

Here we report petrological and major and trace element compositions for a new suite of fresh mantle peridotite xenoliths from TUBAF seamount next to Lihir Island in the New Ireland fore-arc (Papua New Guinea area). The main objectives of this study is to test whether TUBAF peridotites display the typical silica-enrichment signature of SSZ mantle peridotites and how these samples advance our understanding of the origin of this feature and its relevance to global SSZ processes. We show that TUBAF peridotites have experienced very little post-melting metasomatism, and are unique in preserving both silica-enrichment and Fe-Al correlation trends. We present new polybaric flux-melting models of formerly depleted and hybridized (silica-enriched) peridotites in the mantle wedge. Comparison of worldwide SSZ peridotite data with our results on the TUBAF suite suggests that hybridization reactions between pre-depleted mantle and agents derived from the subducted lithosphere ('slab') form excess orthopyroxene (opx) before or during mantle wedge melting. We further use the new data to re-assess earlier interpretations of the origins of TUBAF peridotites.

2. GEOLOGICAL SETTING AND VOLCANISM IN THE NEW HANOVER-NEW IRELAND AND TABAR-LIHIR-TANGA-FENI (TLTF) ARCHIPELAGOS

The New Hanover-New Ireland archipelagos are located northeast of the mainland Papua New Guinea (PNG; Fig. 1). They are composed of Oligocene to Miocene calc-alkaline volcanic rocks generated during subduction of the Pacific plate under the Australian plate along the

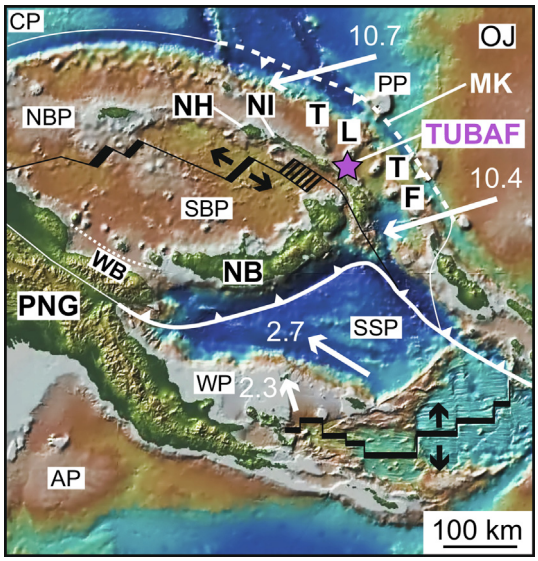

Fig. 1. Tectonic map of the Papua New Guinea area. The active (continuous) and inactive (dashed) convergent margins are indicated with white bold lines, while the spreading centers are in black. Transform faults are indicated with thin white or black lines. White arrows indicate the directions of divergence or convergence with averaged relative velocities given in centimeters per year (Bird, 2003). The now inactive Manus-Kilinailau (MK) trench is located in the top right corner of the map. The opening Manus Basin is composed of the North Bismarck Plate (NBP) and South Bismarck Plate (SBP). TUBAF seamount is indicated with a pink star. Other abbreviations used in the map include: AP, Australian Plate; CP, Caroline Plate; NB, New Britain; NH, Hew Hanover; NI, New Ireland; OJ, Ontong Java plateau; PNG, mainland Papua New Guinea; PP, Pacific Plate; SSP, South Solomon Plate; TLTF, Tabar-Lihir-Tanga-Feni volcanic chain; WB, West Bismarck arc (indicated with a dotted white line); WP, Woodlark Plate.

Manus-Kilinailau trench (Fig. 1; Johnson, 1979; Coleman and Kroenke, 1981). This subduction ceased when the Ontong Java Plateau plugged the trench, but the persistent convergence of the two tectonic plates until today (Bird, 2003) was accommodated by a reversal in subduction polarity (i.e. subduction of Australian plate under the Pacific one; Weissel et al., 1982), and fragmentation into Bismarck microplates during opening of the Manus Basin at ~3.5 Ma (Fig. 1; Taylor, 1979). Collision between New Britain and mainland PNG caused NW-SE transform faulting in the Manus Basin, which was conjugated with NNE-striking extensional faults cutting New Ireland and extending into its fore-arc basin (Fig. 1; Exon et al., 1986). The occurrence of the Pliocene-Pleistocene Tabar-Lihir-Tanga-Feni (TLTF) volcanic chain is directly related to crustal extension in the New Ireland fore-arc basin and the formation of small pull-apart basins (Lindley, 2016).

Volcanism in the TLTF chain started in the Tabar Island group at ~3.6 Ma and migrated to the Lihir, Tanga and Feni Island groups (Fig. 1; Rytuba et al., 1993). Magmas formed in the TLTF chain are unusual at subduction zones. These are mostly silica-undersaturated, high-K calc-alkaline and alkaline rocks (Johnson et al., 1976). These petrological features are more 'akin to' those of magmas from post-collisional or even continental rift environments, but the trace element and radiogenic isotope characteristics of these rocks are, however, 'typical' of subduction zones with elevated Sr, Pb, U, Ba and Rb and depleted Ti, Hf, Zr, Nb and Th (Kennedy et al., 1990; Stracke and Hegner, 1998; Kamenov et al., 2008). The TLTF magma formation models involve adiabatic decompression melting of mantle sources previously modified by Miocene subduction along the Manus-Kilinailau trench (Fig. 1; McInnes and Cameron, 1994; Stracke and Hegner, 1998; Kamenov et al., 2005, 2008).

The TUBAF seamount (3°15.25′S, 152°32.50′E and 1280 m below sea level) is located off the southwestern coast of Lihir Island (Fig. 1). This seamount was discovered and named in 1994 during Sonne cruise SO-94 led by the Technische Universität und Bergakademie Freiberg, which abbreviation is TUBAF. The lava carrying TUBAF ultramafic xenoliths is a volatile-rich, hydrous alkali basalt magma, which typically contains megacrysts of phlogopite and phenocrysts of amphibole and augitic clinopyroxene (cpx) in a vesicular microcrystalline, intersertal matrix (Supplementary Fig. S1; McInnes et al., 2001). The matrix consists of glass containing microlites of amphibole, cpx, plagioclase and magnetite (Fig. S1).

3. EARLIER WORKS ON TLTF PERIDOTITES AND SAMPLE SELECTION

Previous studies of TLTF mantle peridotites have mostly concentrated on samples strongly modified by metasomatic processes occurring in the SSZ lithosphere. These notably include samples containing (i) volatile- and alkali-rich aluminosilicate glasses in partially crystallized interstitial pockets ('SCHARM'; McInnes and Cameron, 1994); (ii) fibrous opx vein networks, generally accompanied by a more pervasive replacement of coarser mantle minerals (re-crystallization) by this fine-grained material (McInnes et al., 2001; Franz et al., 2002; Franz and Romer, 2010); and (iii), coarse/stout pyroxene-rich veins (Franz et al., 2002; Franz and Romer, 2010). Comparatively, little attention has been paid to the coarse-grained paragenesis and bulk-rock major element compositions of TLTF xenoliths. However, McInnes et al. (2001), Grégoire et al. (2001) and Franz et al. (2002) used mineral major and trace element compositions of their least-metasomatized TUBAF peridotites to conclude that these rocks were ancient fragments of Pacific Plate generated at mid-ocean ridges (i.e. abyssal peridotites).

The new TUBAF samples in this study were recovered during the SHAARC cruise, a scientific mission led in the PNG area and Solomon Islands in 2000 by Prof. Brent I. A. McInnes, Prof. Richard J. Arculus and Dr. Gary Massoth on the Franklin vessel. Sampling was performed on the flanks of TUBAF seamount during operations SHDR-08 (3°15.34′S, 152°32.60′E; samples 136309) and SHDR-09 (3°15.34′S, 152°32.67′E; samples 136310), respectively on the 7th and 8th May 2000. In the present study, we have selected only the freshest and largest, coarse-grained peridotites that are homogeneous, i.e. excluding those containing macroscopically visible veins or modal gradations

(Fig. S2). We have deliberately left aside samples displaying fibrous opx and those visibly rich in hydrous minerals such as amphibole or mica (Table 1 and Supplementary Table S1), which are either related to post-melting metasomatism in the SSZ mantle lithosphere, or even very late-stage interactions with the carrier magma during xenolith ascent (e.g. Bénard and Ionov, 2013).

4. ANALYTICAL TECHNIQUES AND MODAL CALCULATIONS

4.1. Major element analyses and modal calculations

High-precision major element data on bulk rocks were acquired by wavelength-dispersive X-ray fluorescence (XRF) spectrometry at J. Gutenberg University, Mainz (Germany), using the techniques outlined by Ionov (2010) and Bénard et al. (2017a). This involved igniting the rock powders for ≥3 h at 1000 °C converting all FeO into Fe_2O_3 and expelling volatiles. Glass beads, produced by fusing 1 g of ignited powders with 5 g of dried LiB_4O_7 (1:6 dilution), were analyzed on a Philips MagiX Pro X-ray sequential spectrometer using ultramafic and mafic reference samples as external standards. Reference samples DZE-1, UB-N, DTS-1 and JP-1 were analyzed as unknowns to control accuracy, with results very close to the recommended values (Table S2). Full duplicate analyses of two peridotite xenoliths are reproduced within ≤0.2 wt% for SiO_2 and MgO, ≤0.07 wt% for FeO_t (i.e. all Fe treated as Fe^{2+}) and CaO, ≤0.01 wt% for Al_2O_3, ≤0.007 wt% for TiO_2, Cr_2O_3, MnO, Na_2O, K_2O, NiO and P_2O_5, and ≤0.0002 for Mg# (Table 2). Peridotite compositions were re-calculated with total Fe as FeO_t to yield the same totals as obtained by XRF for the original analyses, i.e. with total Fe as Fe_2O_3. The same treatment was applied to SSZ peridotites, for which Fe compositions were originally reported as Fe_2O_3 or Fe_2O_3 and FeO (Maury et al., 1992; Parkinson and Pearce, 1998; Pearce et al., 2000; McInnes et al., 2001; Franz et al., 2002).

Major element oxides in peridotite minerals and glasses were determined in polished sections by wavelength-dispersive electron probe micro-analysis (EPMA) with a JEOL 8530-F field-emission instrument at the Institute of Earth Sciences of the University of Lausanne (UNIL, Switzerland, Tables 3, 4 and S3–S13). Nominally-anhydrous mineral analyses were performed at an accelerating voltage of 15 kV and a current of 20 nA as measured with a Faraday cup. Counting times were 10 s and 20 s for Na and K, and 15 s and 30 s for all other elements, respectively on background and peak. Amphibole analyses were performed at a reduced current of 15 nA with counting times of 5 s and 10 s for Cr and Cl, 10 s and 20 s for Ca, Na and K, and 15 s and 30 s for all other elements. Glass analyses were performed at a reduced current of 2 nA with counting times of 5 s and 10 s for Na and K, and 15 s and 30 s for all other elements. In the glass setup, Na and K were analyzed first. Matrix effects were corrected using the Armstrong PRZ oxide correction. Typical 1σ relative standard deviations (RSD) for mineral setups are 0.1–0.5% (Si, Mg and Ca), 0.5–1% (Ti, Al, Fe, Na and K) and 5–20% (Cr, Mn and Ni); they are slightly higher but in the same order of magnitude for the glass setup. The positions of the element peaks were checked at least every ten spots, while standard analyses before and after each analytical session revealed a negligible analytical drift. Modal compositions of the peridotite xenoliths were calculated from XRF and average EPMA data for each sample by mass balance using least-square regressions. Typical 3σ errors for the modal compositions are generally ≤0.6 wt% (Table 1).

4.2. Trace element analyses

Bulk-rock trace element abundances were determined by laser-ablation inductively-coupled-plasma mass-spectrometry (LA-ICP-MS) on the LiB_4O_7 XRF disks (Tables 5 and S14). Analyses were conducted using two Agilent 7700x quadrupole ICP-MS at the Research School of Earth Sciences of the Australian National University (ANU) and at UNIL. The ICP-MS were coupled to either a Lambda Physik COMPex 110 Excimer or a New Wave UP-193FX ArF Excimer LA systems, respectively at ANU and UNIL (λ = 193 nm). Laser ablation was set at a pulse rate of 10 and 20 Hz and an energy fluence of ~12 and ~5 J.cm^{-2}, with spot diameters of 137–233 and 150 μm, respectively at ANU and UNIL. At ANU, counting times were 10 s on the carrier gas (background) followed by 50–60 s for signal and 10–20 s for drop back to background level. At UNIL, counting times were 110 s on the carrier gas (background) followed by 40 s for signal. The NIST 610 and 612 glass standards were used for calibration and ^{29}Si (using XRF data) was used as the internal standard (Jochum et al., 2011). No significant effect on the calculated trace element abundances was observed depending on the choice of a given internal standard or glass standard (NIST 610 or NIST 612; Jochum et al., 2011). The accuracy and precision of the results (expressed as 1σ RSD) were controlled by repeated analyses of NIST 612 and BCR-2G reference materials together with the samples (Gao et al., 2002; Jochum et al., 2005, 2011). The results presented in Table 5 are averages of up to ten spot analyses on each XRF disk, with their reproducibility expressed as 1σ RSD (Table S14). Comparisons of LA-ICP-MS results with those from XRF reveal a good agreement among the two techniques (Fig. S3).

Mineral trace element compositions were determined by LA-ICP-MS in polished sections (Tables S15–S22). Spinel analyses were conducted at ANU using the system described previously, while olivine and pyroxene analyses were conducted at UNIL using an Element XR magnetic-sector ICP-MS coupled to a Australian Scientific Instruments Resolution ArF Excimer LA system (λ = 193 nm). Laser ablation was set at a pulse rate of 5 and 10–20 Hz and an energy fluence of ~12 and 4–6 J.cm^{-2}, with spot diameters of 105 and 50–160 μm, respectively at ANU and UNIL. At ANU, counting times were 30–40 s on the carrier gas (background) followed by 40 s for signal and 10 s for drop back to background level. At UNIL, counting times were 90 s on the carrier gas (background) followed by 25 s for signal and 30–40 s for drop back to background

Table 1
Petrological data.

Sample	Olivine (wt%)	3σ	Opx (wt %)	3σ	Cpx (wt %)	3σ	Spinel (w%)	3σ	Sum	$T_{olivine\text{-}spinel}$ (°C)[a]	$T_{olivine\text{-}spinel}$ (°C)[b]	$T_{opx\text{-}cpx}$ (°C)[c]	$T_{Ca\text{-}in\text{-}opx}$ (°C)[d]	fO_2[e]	fO_2[f]	Comment
136309-1AA	72.0	0.2	23.5	0.3	3.7	0.2	0.80	0.07	100	699	723	830	935	0.03	−0.38	Disseminated f-gr.
136309-1B	67.0	0.3	28.5	0.4	3.7	0.2	0.8	0.1	100	666	693	720	966	−0.27	−0.68	Disseminated f-gr.
136309-1C	74.4	0.4	22.2	0.5	2.7	0.3	0.8	0.1	100	679	705	778	912	−1.16	−1.63	F-gr. at cpx rims
136309-1D	72.3	0.4	24.6	0.5	2.1	0.3	1.1	0.1	100	781	791	711	913	0.55	0.18	Disseminated amph
136309-1E	76.1	0.3	20.7	0.3	2.2	0.2	0.91	0.09	100	734	745	731	936	−0.56	−0.99	Disseminated amph
136310-1AB	71.3	0.1	24.9	0.2	2.9	0.1	0.86	0.04	100	675	688	779	954	−0.41	−0.75	Disseminated amph; f-gr. in cpx pseudomorphs
136310-1AB[g]	71.1	0.1	25.1	0.2	2.93	0.09	0.86	0.04	100	–	–	–	–	–	–	Disseminated amph; f-gr. in cpx pseudomorphs
136310-1AO	75.5	0.2	21.1	0.3	2.5	0.2	0.98	0.08	100	704	725	774	938	0.10	−0.30	Disseminated f-gr.
136310-1AT	81.2	0.4	16.7	0.6	1.4	0.3	0.7	0.2	100	649	679	662	864	−1.24	−1.66	F-gr. at cpx rims
136310-1F	80.1	0.3	16.8	0.4	2.2	0.2	0.99	0.09	100	697	716	792	905	−1.64	−0.01	Disseminated amph
136310-1Q	78.9	0.4	17.5	0.5	2.7	0.3	0.9	0.1	100	665	678	724	928	−0.19	−0.55	F-gr. at cpx rims
136310-1Z	69.4	0.6	26.4	0.9	3.1	0.5	1.1	0.2	100	650	683	745	941	−0.24	−0.77	Disseminated amph; f-gr. at cpx rims
136310-1Z[g]	69.7	0.7	26.3	0.9	2.8	0.5	1.2	0.3	100	–	–	–	–	–	–	Disseminated amph; f-gr. at cpx rims

Opx, orthopyroxene; Cpx, clinopyroxene; F-gr., fine-grained material; Amph, amphibole.

[a] Calculated with the olivine-spinel thermobarometer of O'Neill and Wall (1987) at 1.5 GPa.

[b] Calculated with the olivine-spinel thermobarometer of Ballhaus et al. (1991) at 1.5 GPa.

[c] Calculated with the orthopyroxene-clinopyroxene thermobarometer of Brey and Köhler (1990) at 1.5 GPa.

[d] Calculated with the Ca-in-orthopyroxene thermobarometer of Brey and Köhler (1990) at 1.5 GPa.

[e] Calculated in log units relative to the FMQ redox buffer with the oxybarometer of Wood et al. (1990) and the olivine-spinel thermobarometer of Ballhaus et al. (1991) at 1.5 GPa.

[f] Calculated in log units relative to the FMQ redox buffer with the oxybarometer and the olivine-spinel thermobarometer of Ballhaus et al. (1991) at 1.5 GPa.

[g] Modal calculations using the duplicate bulk rock composition (Table 2).

Table 2
Bulk-rock major element compositions (wt%, except where noted).

Sample	136309-1AA	136309-1B	136309-1C	136309-1D	136309-1E	136310-1AB	136310-1AB[a]	136310-1AO	136310-1AT	136310-1F	136310-1Q	136310-1Z	136310-1Z[a]
SiO_2	44.80	45.21	44.47	44.41	44.11	44.91	44.81	44.03	43.30	43.18	43.47	44.79	44.62
TiO_2	0.006	0.005	0.005	0.003	0.006	0.008	0.007	0.007	0.012	0.010	0.006	0.013	0.013
Al_2O_3	0.76	0.87	0.69	0.53	0.51	0.63	0.64	0.69	0.61	0.59	0.50	0.94	0.93
Cr_2O_3	0.40	0.41	0.35	0.53	0.48	0.48	0.48	0.45	0.31	0.44	0.42	0.47	0.47
FeO_t	8.02	7.76	7.90	8.18	8.15	8.03	7.98	8.46	8.71	8.57	8.50	7.88	7.90
MnO	0.13	0.13	0.12	0.13	0.13	0.13	0.13	0.13	0.13	0.14	0.13	0.12	0.12
MgO	44.76	43.89	45.52	45.02	45.75	44.93	44.77	45.18	46.21	45.98	45.64	44.51	44.49
CaO	1.04	1.13	0.79	0.68	0.69	0.89	0.89	0.74	0.44	0.62	0.78	0.95	0.88
Na_2O	b.d.	b.d.	0.004	0.011	0.003	0.027	0.028	0.029	0.019	0.009	0.027	0.026	0.019
K_2O	b.d.	b.d.	b.d.	0.010	b.d.	0.010	0.010	0.020	0.010	0.010	0.010	0.010	b.d.
NiO	0.30	0.29	0.31	0.30	0.30	0.29	0.29	0.30	0.30	0.31	0.31	0.30	0.30
P_2O_5	b.d.	b.d.	b.d.	0.001	b.d.	0.007	0.007	0.008	0.008	0.001	0.008	0.006	0.007
Total	100.21	99.70	100.17	99.83	100.15	100.33	100.04	100.04	100.06	99.85	99.80	100.02	99.74
LOI	−0.32	−0.06	−0.02	0.19	−0.32	−0.50	−0.51	−0.47	−0.53	−0.17	−0.60	−0.53	−0.51
V (ppm)	–	–	–	–	–	40	41	43	30	–	37	43	46
Co (ppm)	116	111	113	116	113	117	117	116	127	123	124	118	115
Zn (ppm)	–	–	–	–	–	42	40	50	43	–	46	44	45
Mg#	0.909	0.910	0.911	0.907	0.909	0.909	0.909	0.905	0.904	0.905	0.905	0.910	0.909

b.d., below detection limit.
FeO_t, all Fe treated as Fe^{2+}.
LOI, loss of ignition (3h at 1000°C, negative values mean mass gain on ignition).
Mg#, $Mg/(Mg+Fe_t)$.
[a] Duplicate analysis.

Table 3
Average major element compositions of coarse minerals (wt%).

Sample	136309-1AA	136309-1B	136309-1C	136309-1D	136309-1E	136310-1AB	136310-1AO	136310-1AT	136310-1F	136310-1Q	136310-1Z
Mineral	Olivine	Olivine	Olivine	Olivine	Olivine	Olivine	Olivine	Olivine	Olivine	Olivine	Olivine
Comment	Cores & rims; n = 41	Cores & rims; n = 21	Cores & rims; n = 39	Cores & rims; n = 24	Cores & rims; n = 38	Cores & rims; n = 18	Cores & rims; n = 44	Cores & rims; n = 32	Cores & rims; n = 34	Cores & rims; n = 23	Cores & rims; n = 18
SiO_2	40.77	40.64	40.75	40.81	40.77	40.78	40.63	40.70	40.59	40.68	40.61
TiO_2	0.01	0.01	0.01	0.01	0.00	0.01	0.01	0.01	0.01	0.01	0.01
Al_2O_3	0.01	0.02	0.01	0.01	0.01	0.01	0.01	0.01	0.01	0.01	0.01
Cr_2O_3	0.03	0.03	0.04	0.01	0.01	0.02	0.02	0.01	0.02	0.02	0.02
FeO_t	8.76	8.59	8.44	8.79	8.70	8.81	9.03	9.02	9.01	8.91	8.33
MnO	0.13	0.13	0.13	0.13	0.13	0.13	0.14	0.13	0.14	0.13	0.12
MgO	49.83	49.88	50.01	50.08	50.03	49.93	49.50	49.43	49.64	49.52	50.03
CaO	0.01	0.02	0.01	0.03	0.02	0.02	0.01	0.01	0.01	0.02	0.02
Na_2O	–	–	0.00	–	–	–	–	–	–	–	–
K_2O	–	–	0.01	–	–	–	–	–	–	–	–
NiO	0.39	0.40	0.40	0.39	0.38	0.38	0.38	0.37	0.37	0.38	0.41
Total	99.92	99.69	99.76	100.23	100.04	100.07	99.71	99.68	99.78	99.67	99.53
Mg#	0.910	0.912	0.914	0.910	0.911	0.910	0.907	0.907	0.908	0.908	0.915
Mineral	Orthopyroxene	Orthopyroxene	Orthopyroxene	Orthopyroxene	Orthopyroxene	Orthopyroxene	Orthopyroxene	Orthopyroxene	Orthopyroxene	Orthopyroxene	Orthopyroxene
Comment	Cores & rims; n = 30	Cores & rims; n = 28	Cores & rims; n = 20	Cores & rims; n = 23	Cores & rims; n = 30	Cores & rims; n = 30	Cores & rims; n = 14	Cores & rims; n = 12	Cores & rims; n = 20	Cores & rims; n = 28	Cores & rims; n = 30
SiO_2	56.96	56.41	56.91	56.91	57.26	56.78	56.84	56.49	56.97	56.79	56.30
TiO_2	0.01	0.01	0.01	0.01	0.02	0.01	0.02	0.03	0.02	0.01	0.03
Al_2O_3	1.77	1.86	1.69	1.14	1.27	1.40	1.65	2.11	1.54	1.31	2.03
Cr_2O_3	0.40	0.42	0.41	0.34	0.37	0.39	0.38	0.50	0.38	0.34	0.45
FeO_t	5.96	5.84	5.70	5.90	5.81	5.86	6.22	6.13	6.05	6.09	5.82
MnO	0.15	0.15	0.14	0.15	0.15	0.15	0.15	0.16	0.16	0.16	0.14
MgO	34.36	34.40	34.62	34.88	34.67	34.54	34.28	34.16	34.51	34.39	34.32
CaO	0.61	0.70	0.54	0.54	0.61	0.66	0.61	0.43	0.52	0.58	0.62
Na_2O	0.01	0.01	0.01	0.01	0.01	0.01	0.01	0.01	0.01	0.00	0.01
K_2O	0.01	0.01	0.01	0.01	0.01	0.01	–	–	–	0.01	0.00
NiO	0.08	0.08	0.08	0.08	0.07	0.07	0.07	0.07	0.07	0.07	0.08
Total	100.30	99.86	100.11	99.95	100.24	99.87	100.23	100.08	100.23	99.74	99.79
Mg#	0.911	0.913	0.915	0.913	0.914	0.913	0.908	0.909	0.911	0.910	0.913
Cr#	0.130	0.127	0.134	0.162	0.158	0.155	0.132	0.137	0.143	0.144	0.128
Mineral	Clinopyroxene	Clinopyroxene	Clinopyroxene	Clinopyroxene	Clinopyroxene	Clinopyroxene	Clinopyroxene	Clinopyroxene	Clinopyroxene	Clinopyroxene	Clinopyroxene
Comment	Cores & rims; n = 23	Cores & rims; n = 28	Cores & rims; n = 20	Cores & rims; n = 27	Cores & rims; n = 29	Cores & rims; n = 30	Cores & rims; n = 14	Cores & rims; n = 12	Cores & rims; n = 14	Cores & rims; n = 27	Cores & rims; n = 30
SiO_2	53.89	53.41	53.70	53.90	54.15	53.75	54.11	53.82	53.74	53.97	53.49
TiO_2	0.02	0.02	0.02	0.01	0.03	0.02	0.03	0.10	0.06	0.02	0.07
Al_2O_3	2.09	1.95	1.89	1.26	1.53	1.47	1.75	1.95	1.99	1.35	2.13
Cr_2O_3	0.76	0.68	0.70	0.63	0.78	0.62	0.64	0.67	0.78	0.55	0.69
FeO_t	2.09	1.93	1.79	1.89	1.88	1.87	2.04	1.78	2.08	1.98	1.94
MnO	0.07	0.07	0.07	0.07	0.08	0.07	0.08	0.07	0.08	0.07	0.07

MgO	17.54	17.59	17.63	17.85	17.53	17.79	17.56	17.33	17.44	17.76	17.51
CaO	24.03	24.56	24.26	24.36	24.40	24.19	24.31	24.85	24.13	24.45	24.43
Na_2O	0.11	0.05	0.08	0.19	0.18	0.08	0.12	0.07	0.14	0.11	0.09
K_2O	0.01	0.00	0.00	0.00	0.01	0.00	–	–	–	0.00	0.01
NiO	0.05	0.04	0.04	0.04	0.04	0.04	0.04	0.04	0.04	0.04	0.05
Total	100.57	100.26	100.11	100.08	100.49	99.87	100.68	100.68	100.48	100.24	100.42
Mg#	0.937	0.942	0.946	0.944	0.943	0.944	0.939	0.946	0.937	0.941	0.941
Cr#	0.193	0.187	0.197	0.243	0.250	0.217	0.195	0.184	0.207	0.212	0.175
Mineral	Spinel	Spinel	Spinel	Spinel	Spinel	Spinel	Spinel	Spinel	Spinel	Spinel	Spinel
Comment	Cores & rims; n = 18	Cores & rims; n = 18	Cores & rims; n = 15	Cores & rims; n = 18	Cores & rims; n = 16	Cores & rims; n = 17	Cores & rims; n = 12	Cores & rims; n = 14	Cores & rims; n = 12	Cores & rims; n = 10	Cores & rims; n = 12
SiO_2	0.01	0.01	0.02	0.02	0.01	0.01	0.02	0.02	0.03	0.00	0.01
TiO_2	0.03	0.02	0.02	0.03	0.06	0.04	0.04	0.07	0.09	0.04	0.06
Al_2O_3	28.48	30.47	30.33	20.05	22.31	23.67	27.40	32.95	26.01	23.48	33.57
Cr_2O_3	38.77	37.12	38.48	46.78	46.12	44.04	39.90	35.22	41.08	43.58	34.16
FeO_t	18.46	18.00	16.73	20.15	18.59	20.11	19.34	17.42	19.81	20.81	17.06
MnO	0.13	0.12	0.11	0.14	0.14	0.16	0.14	0.13	0.13	0.16	0.11
MgO	13.18	13.36	13.73	12.06	12.10	11.36	12.76	13.54	12.29	10.97	14.20
CaO	0.01	0.03	0.01	0.01	0.02	0.00	0.03	0.01	0.01	0.01	0.01
Na_2O	–	–	–	–	–	–	–	–	–	–	–
K_2O	–	–	–	–	–	–	–	–	–	–	–
NiO	0.11	0.10	0.10	0.08	0.07	0.07	0.08	0.10	0.10	0.07	0.12
Total	99.16	99.22	99.50	99.29	99.41	99.46	99.68	99.46	99.55	99.13	99.29
Mg#	0.560	0.569	0.594	0.516	0.537	0.502	0.540	0.581	0.525	0.484	0.597
Cr#	0.477	0.450	0.460	0.610	0.581	0.555	0.494	0.418	0.515	0.555	0,406

b.d., below detection limit.
FeO_t, all Fe treated as Fe^{2+}.
Mg#, $Mg/(Mg+Fe_t)$.
Cr#, Cr/(Cr+Al).

Table 4
Average major element compositions of disseminated amphibole (wt%, except where noted).

Sample	136309-1D	136309-1E	136309-1AB	136310-1F	136310-1Z
Mineral	Tremolitic hornblende	Mg-hornblende	Mg-hornblende	Mg-hornblende	Mg-hornblende
Comment	Cores & rims; n = 4	Cores & rims; n = 15	Cores & rims; n = 3	Cores & rims; n = 12	Cores & rims; n = 11
SiO_2	53.58	50.59	51.15	51.32	50.53
TiO_2	0.04	0.15	0.11	0.22	0.26
Al_2O_3	4.86	8.39	8.13	7.84	8.83
Cr_2O_3	1.28	1.71	1.60	1.18	1.22
FeO_t	2.50	2.61	2.77	2.61	2.69
MnO	0.03	0.05	0.05	0.05	0.04
MgO	21.99	20.17	20.15	20.33	19.89
CaO	12.59	12.75	12.77	12.91	12.98
Na_2O	1.58	1.54	1.04	1.14	1.15
K_2O	0.11	0.02	0.01	0.01	0.01
NiO	0.09	0.10	0.08	0.09	0.10
Cl (ppm)	41	100	81	71	103
Total	98.64	98.08	97.87	97.70	97.71
Mg#	0.940	0.932	0.928	0.933	0.929
Cr#	0.145	0.120	0.117	0.089	0.085

FeO_t, all Fe treated as Fe^{2+}.
Mg#, Mg/(Mg+Fe_t).
Cr#, Cr/(Cr+Al).

level. All UNIL procedures included pre-ablation cleaning of the sample surface with spot diameters of 100–240 μm. The NIST 610 and 612 glass standards were used for calibration, with ^{53}Cr and ^{29}Si (both using EPMA data) as the internal standards, respectively at ANU and UNIL (Jochum et al., 2011). For all mineral trace element analyses, the accuracy and precision (expressed as 1σ RSD) of the results, were controlled by repeated analyses of NIST 612 and BCR-2G reference materials together with the samples (Gao et al., 2002; Jochum et al., 2005, 2011). Results presented in Tables S15–S18 allowed us calculating averages of up to eight spot analyses for each coarse mineral in a given sample, with their reproducibility expressed as 1σ RSD.

5. RESULTS

5.1. Petrographical observations and modal compositions

All TUBAF xenoliths in this study are fresh, coarse-grained spinel peridotites with protogranular texture (Figs. 2a and b, S4, S5 and Table 1). Both opx and cpx typically occur as coarse grains; the former mineral frequently encloses rounded olivine while the smallest grains of the latter are sometimes associated with spinel (Figs. 2a and c, S4 and S5). Both opx and cpx display straight (euhedral) to lobate (anhedral to rounded) grain boundaries with olivine and systematically contain exsolutions, with some evidence for plastic deformation (Figs. 2a–e, S4 and S5). Spinel is found as small euhedral and large anhedral grains (Figs. 2b, c and f, S4 and S5). Amphibole disseminated in the coarse-grained matrix is rarely found as small subhedral grains, which are generally associated with cpx, and less frequently opx (Figs. 2a, S4 and S5).

Fine-grained, acicular cpx and opx in vug-bearing glass surrounds larger, anhedral relics of amphibole, which altogether form pockets that sometimes partially replace the rims of coarse cpx (Figs. 2a and d, S4 and S5). Rounded olivine relics are rarely identified in the pockets. In some cases, fine-grained pockets fill pseudomorphs of former coarse cpx and only isolated relics of this mineral remain (Fig. S5). Pyroxenes in the fine-grained pockets appear darker and display some evidence for intra-crystal chemical zoning in back-scattered electron (BSE) images, whereas the coarse-grained matrix does not (Figs. 2a and d, S4 and S5). We do not identify any preferential distribution of the fine-grained pockets in relation to the carrier magma.

Modal calculations using coarse minerals show that TUBAF peridotites are characterized by relatively low cpx abundances (≤4 wt%) associated with variable opx contents (Fig. 3 and Table 1). Orthopyroxene contents notably extend to 'high' proportions with some rocks containing up to ~30 wt% opx (Fig. 3). In this study, 'high' opx implies ≥24 wt% opx at 0–5 wt% cpx, which is the upper end predicted for harzburgite residues of ≥25% of anhydrous melting of fertile lherzolite (i.e. PM- or DMM-like) at ≤2 GPa, using experimental melting reactions (Figs. 3 and S6; Kinzler and Grove, 1992; Baker and Stolper, 1994; Walter and Presnall, 1994; Walter et al., 1995; Kinzler, 1997; Walter, 1998; Parman and Grove, 2004). A limit of ~22 wt% opx was previously considered for hydrous melting by Bénard et al. (2017a), as adding H_2O depletes spinel harzburgite residues by ≥2 wt% opx for an otherwise similar set of conditions (Fig. S6; Hirose and Kawamoto, 1995; Gaetani and Grove, 1998). When including the compositions of the rare disseminated amphibole grains, modal calculations systematically return either negative values or ≤1 wt% for the abundances of this mineral (Table S1).

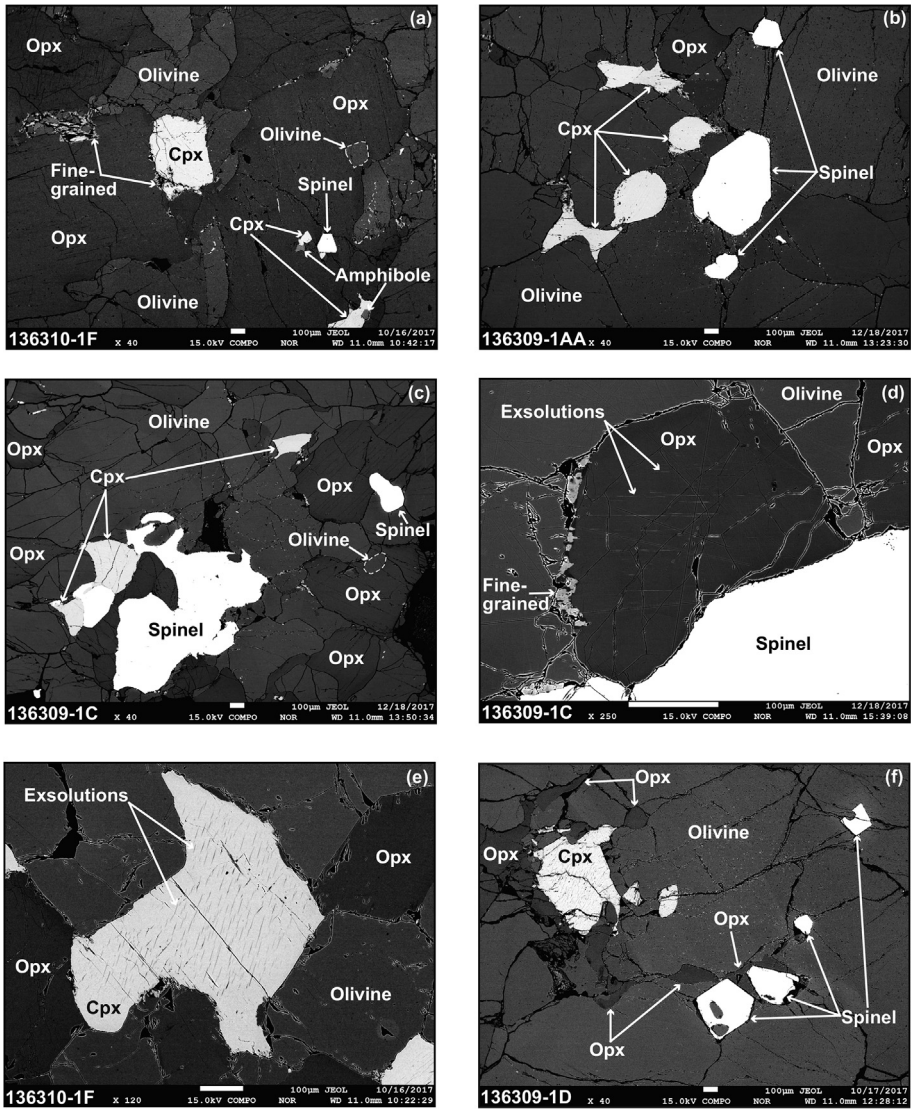

Fig. 2. Back-scattered electron images for TUBAF peridotites in this study. Sample names are indicated on the lower left corners of the images. Scale bar at the bottom of the images is 100 μm. (a–e) Coarse orthopyroxene (opx), clinopyroxene (cpx) and spinel display variable sizes and straight (euhedral) to lobate or irregular (anhedral) grain boundaries, with both pyroxenes containing exsolutions. (a, c) Small olivine grains can occur as rounded inclusions in coarse opx. (c, f) Coarse opx can be also found as euhedral or elongated interstitial grains. (a) In most samples, small euhedral grains of disseminated amphibole and fine-grained pockets are rare; both are associated with coarse cpx, which they partially replace. No evidence for intra-crystal chemical zoning is observed in the coarse-grained matrix.

No relationship between modal compositions and the abundances of fine-grained pockets is observed.

5.2. Major element compositions

Bulk compositions of TUBAF peridotites in this study are characterized by a combination of high Cr_2O_3 (≥0.3 wt%), MnO (≥0.12 wt%) and NiO (≥0.28 wt%) contents (i.e. moderately incompatible to compatible minor elements; Fig. 4a–c and Table 2). Compared to the major element trends for melting residues of fertile KR-4003 lherzolite (Herzberg, 2004), TUBAF peridotites define a Fe-Al correlation from ~2 to <1 GPa along the 25–30% melting isopleths (Fig. 5a). The rocks also display the typical SSZ silica-enrichment trend in comparison with KR-4003 residues; this trend is evaluated for a given melting degree (F), as monitored by Al_2O_3 and MgO contents (Fig. 5b and c). In addition, a robust Si-Mg correlation following 25–30% melting isopleths characterizes TUBAF peridotites (Fig. 5c). The rocks are also highly depleted in the incompatible major element oxides Al_2O_3, TiO_2, Na_2O and K_2O, similar to other residual SSZ peridotites (Fig. 5d–f).

The composition of coarse minerals (Tables 3, 4 and S3–S6) is homogeneous at the grain scale for nearly all TUBAF peridotites in this study (Fig. S7). Only slight systematic core-to-rim variations include lower CaO (opx), and higher Mg# (Mg/[Mg+∑Fe], where ∑Fe refers to Fe^{3+}+Fe^{2+}) and lower Cr# (Cr/[Cr + Al]) at rims (cpx and spinel;

Table 5
Average trace element abundances in bulk rocks (ppm, except where noted).

Sample	136309–1AA	136309–1B	136309-1C	136309–1D	136309-1E	136310–1AB	136310–1AB[a]	136310–1AO	136310–1AT	136310–1F	136310–1Q	136310–1Z	136310–1Z[a]
Comment	n = 3–5	n = 4–5	n = 4–5	n = 4–5	n = 4–5	n = 4–5	n = 5	n = 5	n = 5	n = 4–5	n = 5	n = 5	n = 5
Al_2O_3 (wt%)	0.76	0.86	0.75	0.55	0.52	0.64	0.65	0.72	0.62	0.59	0.53	0.96	0.96
CaO (wt%)	1.06	1.16	0.84	0.70	0.71	0.93	0.92	0.96	0.47	0.64	0.83	1.01	0.92
Sc	14	15	10	13	13	14	14	14	9.62	11	12	12	12
Ti	29	26	22	21	40	30	29	31	63	58	24	73	74
V	53	59	43	53	47	51	50	50	33	47	43	51	50
Cr	2687	2773	2362	3585	3344	3251	3228	3047	2048	2937	2796	3148	3071
Mn	963	940	907	976	1005	975	961	961	963	997	953	895	890
Co	114	108	114	114	117	112	111	111	120	120	117	111	111
Ni	2314	2186	2363	2313	2102	2276	2249	2249	2323	2350	2385	2305	2315
Cu	21	13	30	29	34	8.88	8.65	8.65	8.69	39	6.26	6.46	8.55
Zn	41	40	42	47	48	43	43	43	48	47	50	50	47
Rb	0.045	0.038	0.047	0.300	0.075	0.241	0.231	–	0.239	0.247	0.195	0.246	0.113
Sr	0.246	0.184	0.288	1.67	0.262	0.583	0.590	–	0.381	1.12	0.967	0.441	0.431
Y	0.106	0.089	0.073	0.056	0.093	0.101	0.102	–	0.128	0.145	0.092	0.137	0.133
Zr	0.111	0.064	0.114	0.196	0.169	0.163	0.165	–	0.104	0.218	0.226	0.100	0.096
La	0.0041	0.0043	0.0084	0.019	0.0082	0.012	0.011	–	0.0061	0.021	0.017	0.0095	0.0080
Ce	0.0083	0.0087	0.012	0.045	0.015	0.023	0.022	–	0.017	0.039	0.029	0.015	0.012
Pr	0.0015	0.0011	0.0009	0.0045	0.0015	0.0043	0.0043	–	0.0034	0.0046	0.0040	0.0019	0.0019
Nd	0.0067	0.0042	0.0040	0.017	0.0051	0.018	0.016	–	0.0061	0.017	0.018	0.0095	0.0075
Sm	0.0027	0.0022	b.d.	0.0054	0.0017	0.0077	0.0059	–	0.0035	0.0033	0.0065	0.0024	0.0029
Eu	0.0012	0.0009	b.d.	0.0017	0.0009	0.0024	0.0019	–	0.0034	0.0014	0.0016	0.0008	0.0008
Gd	b.d.	b.d.	0.0032	0.0051	0.0042	0.0084	0.0082	–	0.0094	0.0061	0.0059	0.0049	0.0040
Tb	0.0012	0.0008	0.0007	0.0008	0.0008	0.0018	0.0016	–	0.0018	0.0015	0.0013	0.0011	0.0012
Dy	0.0098	0.0078	0.0064	0.0079	0.0094	0.012	0.012	–	0.017	0.014	0.011	0.013	0.014
Ho	0.0034	0.0030	0.0021	0.0022	0.0030	0.0038	0.0035	–	0.0055	0.0046	0.0036	0.0043	0.0046
Er	0.014	0.015	0.0082	0.0089	0.013	0.014	0.015	–	0.029	0.019	0.013	0.022	0.022
Tm	0.0029	0.0033	0.0024	0.0019	0.0029	0.0036	0.0034	–	0.0059	0.0038	0.0028	0.0049	0.0041
Yb	0.031	0.032	0.025	0.018	0.027	0.031	0.031	–	0.048	0.034	0.026	0.042	0.041
Lu	0.0072	0.0078	0.0051	0.0040	0.0064	0.0063	0.0062	–	0.0087	0.0069	0.0050	0.0090	0.0083

b.d., below detection limit.
[a] Duplicate analysis.

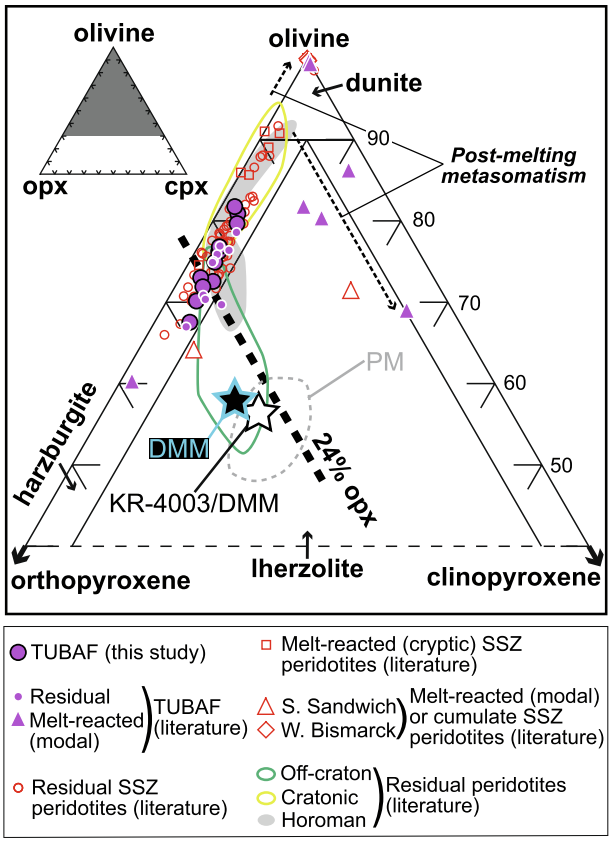

Fig. 3. Olivine-opx-cpx triangular plot of the modal compositions of TUBAF peridotites in this study (large pink dots with black borders). Also shown for comparison are data for (i) TUBAF peridotites from the literature (small pink dots and triangles with white borders; McInnes et al., 2001; Franz et al., 2002); (ii) residual (small red circles) and melt-reacted (cryptic metasomatism; small red squares) supra-subduction zone (SSZ) peridotites from the Izu-Bonin-Mariana (Parkinson and Pearce, 1998), Kamchatka (Ionov, 2010) and West Bismarck (Bénard et al., 2017a) arcs; (iii) melt-reacted SSZ peridotites (modal metasomatism) from the South Sandwich fore-arc (white triangles with red borders; Pearce et al., 2000) and West Bismarck arc (white diamonds with red borders; Bénard et al., 2017a); and (iv) residual spinel peridotites from the Horoman Massif (grey field; Takazawa et al., 1996, 2000) and off-craton continental (green contour and/or dots; Ionov, 2004, 2007; Ionov and Hofmann, 2007) and cratonic (yellow contour and/or dots; Doucet et al., 2012) tectonic settings. Also shown are the modal compositions modelled at 1.25–1.5 GPa in this study for the fertile KR-4003 lherzolite (Walter, 1998) with depleted mid-ocean ridge basalt mantle (DMM; Salters and Stracke, 2004) TiO_2, Cr_2O_3, MnO, Na_2O, K_2O and NiO contents ('KR-4003/DMM', white star with black border), as well as modal estimates for the DMM (black star with light-blue border; Workman and Hart, 2005) and the primitive mantle (dotted grey contour; Wittig et al., 2008). F, melting degree. Other symbols and acronyms are as in Fig. 2. (For interpretation of the references to colour in this figure legend, the reader is referred to the web version of this article.)

Fig. S7). Coarse minerals have elevated Mg# ranging from 0.905 to 0.915 in olivine containing high MnO and NiO (≥0.1 and ≥0.3 wt%, respectively), and from 0.905 to 0.95 in pyroxenes containing very low TiO_2, Al_2O_3 and alkalis (e.g. ≤0.2 wt% TiO_2 and Na_2O in cpx; Figs. 6a–e and S8). Spinel in TUBAF peridotites is characterized by low TiO_2 (≤0.1 wt%) and a Cr# ranging from 0.35 to 0.65 (Figs. 6f and S8). The compositions of coarse minerals in TUBAF peridotites are very similar to those in other residual SSZ peridotites, as it is the case for bulk-rock data (Figs. 6 and S8).

The compositional range of pyroxenes in fine-grained pockets is typically wider than for the coarse-grained ones, which is consistent with evidence from BSE imaging (Fig. S9 and Tables S9 and S10). These fine-grained pyroxenes tend to have higher Mg# (up to 0.96) and Cr_2O_3 for a given Al_2O_3 relative to their coarse-grained counterparts, but this is not the case for olivine, which present indistinguable compositions (Fig. S9 and Table S8). The compositions of amphibole are similar whether this mineral is present as relics in the fine-grained pockets (tremolitic- and Mg-hornblende) or as disseminated grains in the coarse-grained matrix (mostly Mg-hornblende; Fig. S9 and Tables 4, S7 and S11). Glass analyses in the fine-grained pockets were only possible in 136310-1F, where it is dacitic with low TiO_2 (~0.1 wt%) and total alkalis (≤3 wt% $Na_2O + K_2O$) but elevated Mg# (~0.50; Table S12). Neither cpx nor amphibole in TUBAF peridotites have major element compositions comparable to those of the same minerals in their carrier magma (Table S13).

5.3. Trace element abundances

Trace elements in bulk TUBAF peridotites in this study form a consistent field with the PM-normalized (McDonough and Sun, 1995) abundances of the moderately incompatible rare-earth elements (REE) decreasing monotonously from heavy REE (HREE) to middle REE (MREE; Fig. 7a and Table S14). The abundances of these REE are very low, as they typically range from 0.002 to 0.1 times those inferred for PM (Fig. 7a). When normalized to PM values (indicated with a subscript 'N'), the moderately incompatible high-field strength elements (HFSE, e.g. Ti and Zr) appear enriched relative to MREE, as do highly incompatible elements such as light REE (LREE) and large-ion lithophile elements (LILE; e.g. Sr and Rb; Fig. 7a). Taken collectively, these features form characteristically 'U-shaped' trace element patterns with positive anomalies in some HFSE and positive 'spikes' in fluid-mobile elements (Fig. 7a). Positive correlations are observed between the abundances of HREE and Al_2O_3 in bulk TUBAF peridotites (e.g. Lu; Fig. 7b). These correlations become weaker for less compatible REE (Fig. 7b and c), and then negative for REE more incompatible than Tb, but also for fluid-mobile elements or HFSE (e.g. Zr; Fig. 7d).

Trace element abundances in coarse minerals are consistent from one grain to another when considering a given sample (Tables S15–S18). We note that, despite the presence of exsolutions, the average CaO contents of pyroxenes for a given sample are similar whether these are analyzed by EPMA or LA-ICP-MS (Tables S4, S5, S16 and S17). Trace element patterns of coarse minerals replicate the monotonous decrease from HREE to MREE of the bulk rocks

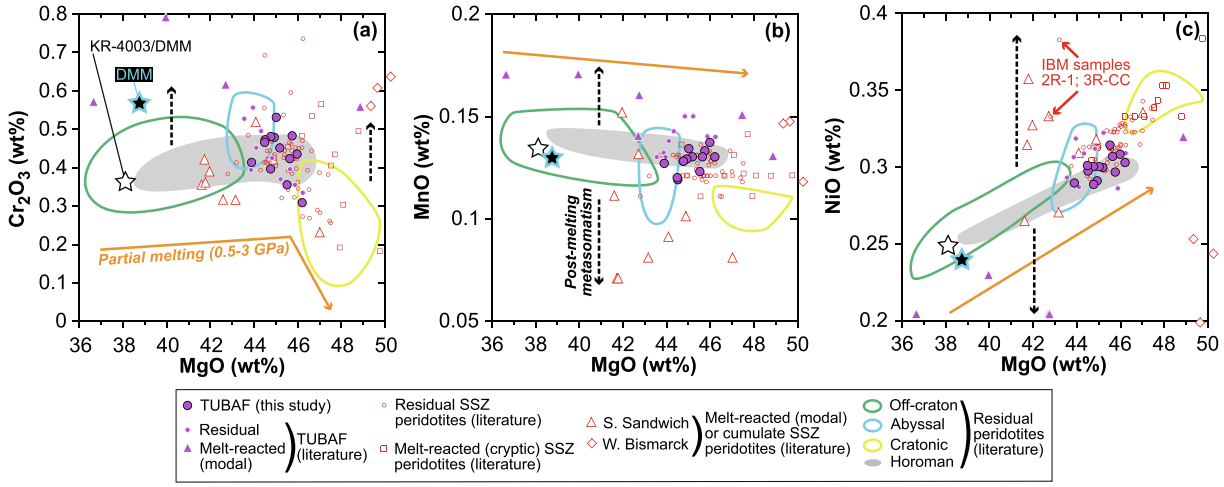

Fig. 4. Co-variation plots of major element oxide compositions (in wt%) of bulk TUBAF peridotites in this study. Also shown for comparison are data for residual spinel peridotites from the Mid-Atlantic Ridge (light-blue contour and/or dots; Stephens, 1997). IBM, Izu-Bonin-Mariana. The melt-reacted (cryptic) versus residual sample classification for SSZ peridotite literature data relies on the conclusions in the original publications. However, note that some rare samples originally classified as residual could also be affected by cryptic post-melting modifications (IBM samples 2R-1 and 3R-CC from their major element contents; Parkinson and Pearce, 1998, and Kamchatka samples Av1 and Av16 from their trace element abundances; Ionov, 2010). Other symbols and acronyms are as in Figs. 2 and 3.

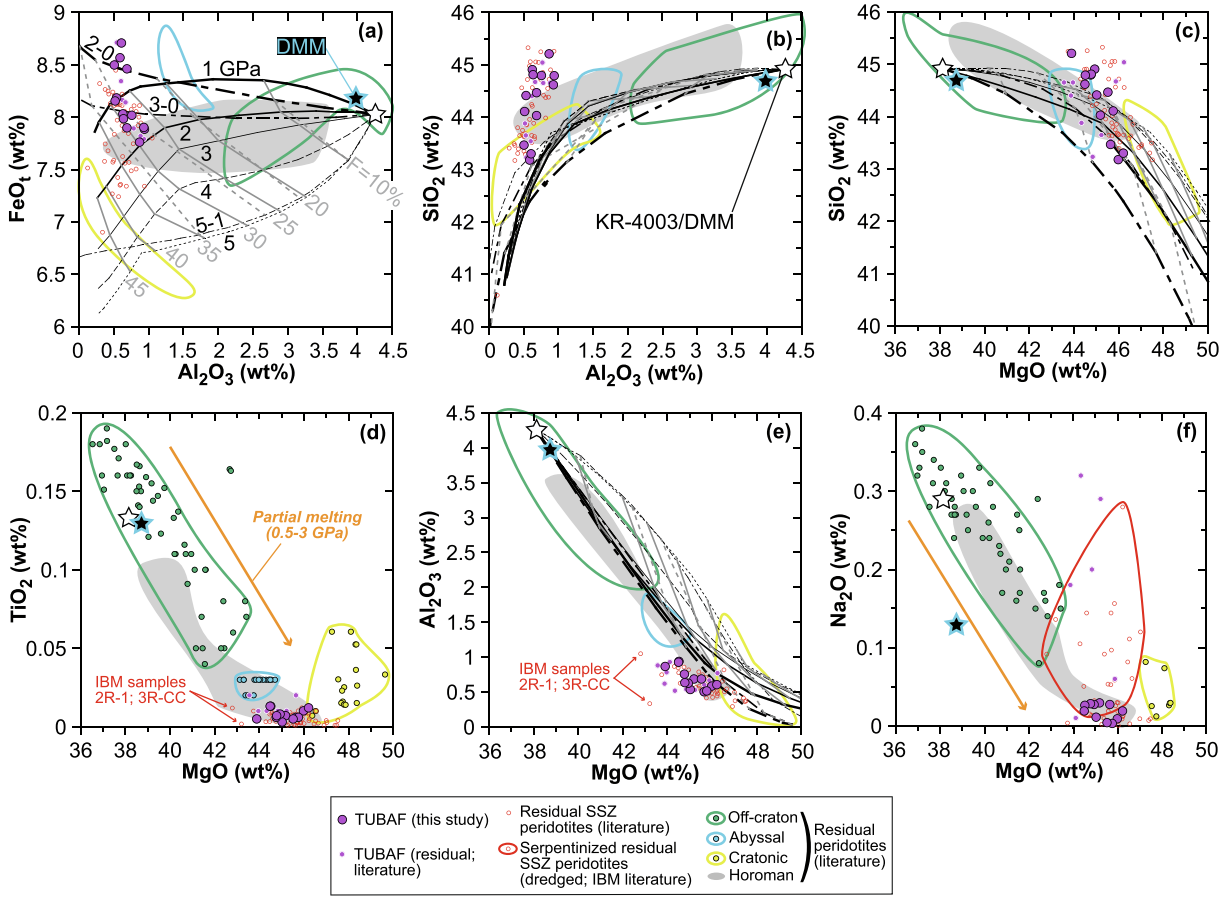

Fig. 5. Co-variation plots of major element oxide compositions (in wt%) of bulk TUBAF peridotites in this study. Also shown for comparison in (a–c) and (e) are trends for the melting residues of the fertile KR-4003 lherzolite (Walter, 1998), as reported in Herzberg (2004). These residue trends are indicated with black lines for isobaric melting (1–5 GPa) and decompression melting (2–0, 3–0 and 5–1 GPa). Also shown are the melting-degree isopleths for isobaric (continuous grey lines) and decompression (dashed grey lines) melting. FeO_t, all Fe treated as Fe^{2+}. Other symbols and acronyms are as in Figs. 2–4.

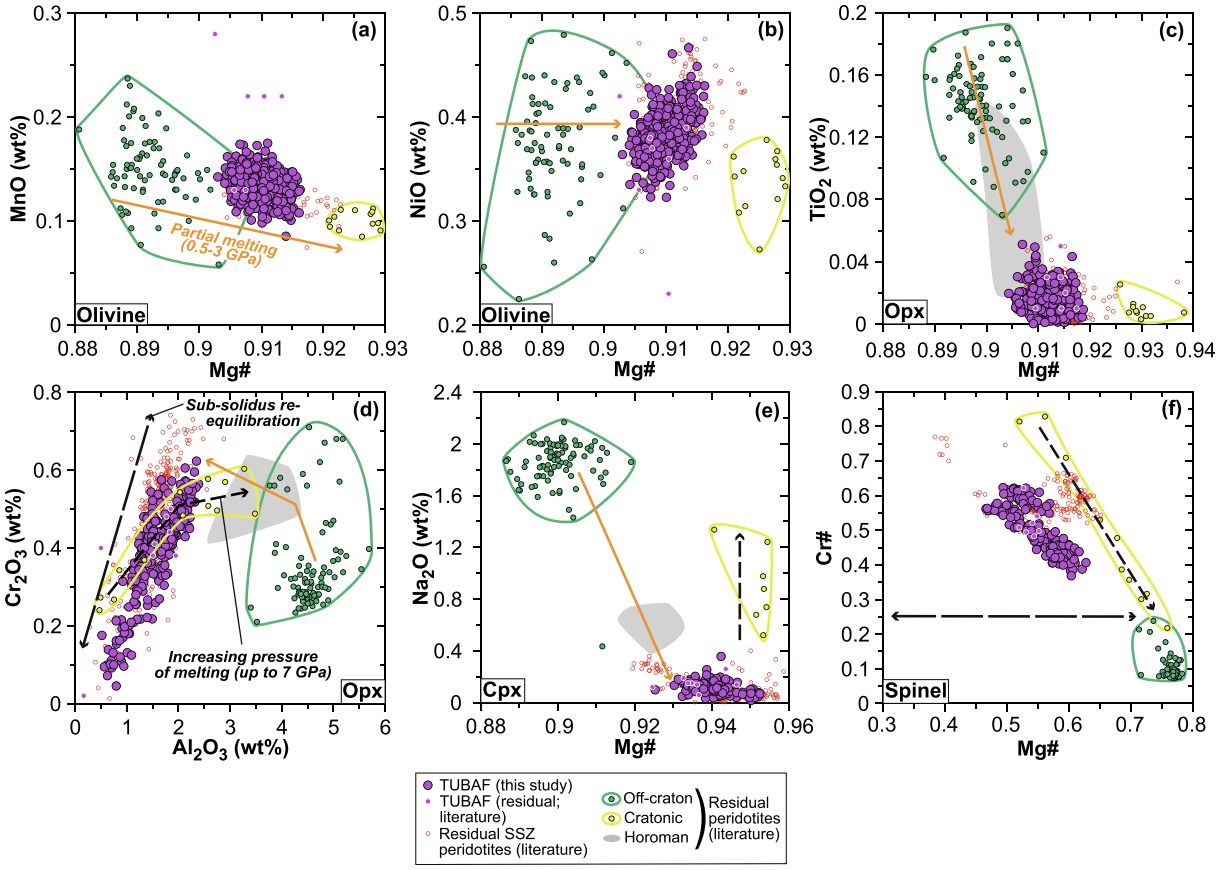

Fig. 6. Co-variation plots of major element oxide compositions (in wt%), Mg# (Mg/[Mg+∑Fe], where ∑Fe refers to Fe^{3+}+Fe^{2+}) and Cr# (Cr/[Cr + Al]) of coarse minerals in TUBAF peridotites in this study. Other symbols and acronyms are as in Figs. 2–5.

(Fig. 8a–c). However, opx generally display a more restricted range in the abundances of MREE and some LREE than cpx (Fig. 8b and c). Amphibole and bulk fine-grained pockets (opx + cpx + glass aggregates) have trace element patterns very similar to those of the neighbouring coarse cpx they partially replace, with the notable exception of positive spikes in fluid-mobile elements (e.g. Pb, Ba and Rb; Fig. S10 and Tables S19–S21). Neither cpx nor amphibole in TUBAF peridotites have trace element patterns comparable to those of the same minerals in their carrier magma (Fig. S11 and Table S22).

5.4. Thermobarometric and oxygen fugacity estimates

Calculations using olivine-spinel geothermometers (O'Neill and Wall, 1987; Ballhaus et al., 1991) assuming a pressure of 1.5 GPa give a temperature range of 650–790 °C for the equilibration of TUBAF peridotites, with an average of 701 ± 37 °C (1σ; Table 1). Temperatures calculated using the opx-cpx geothermometer of Brey and Köhler (1990) at 1.5 GPa give results overlapping within ± 10% with those obtained using the olivine-spinel method (750 ± 46 °C, 1σ; Fig. 9a). However, this is not the case for the Ca-in-opx geothermometer (Brey and Köhler, 1990), which returns significantly higher temperatures (926 ± 27 °C, 1σ; Fig. 9b). Using the parameterization of Witt-Eickschen and O'Neill (2005), REE partitioning systematics between coarse pyroxenes are consistent with equilibration conditions of ~1000 °C for all peridotites (Fig. 9c). Taken collectively, these estimates provide a wide temperature spectrum from ~1000 °C (REE partitioning) and 900–970 °C (Ca-in-opx) to ~700 °C (olivine-spinel and opx-cpx; Fig. 9d). Oxygen fugacity (fO_2) conditions calculated on the basis of spinel stoichiometry, using the oxybarometer of Wood et al. (1990) and the olivine-spinel temperatures at 1.5 GPa (Ballhaus et al., 1991), range from −1.6 to 0.6 log units relative to the fayalite-magnetite-quartz (FMQ) redox buffer, with an average of −0.5 ± 0.7 (1σ; Table 1).

6. DISCUSSION

6.1. Minor post-melting metasomatism in the TUBAF peridotites in this study: Localized amphibole formation and decompression-induced breakdown

Traces of (TiO_2, Na_2O, K_2O)-bearing Mg-hornblende disseminated in the coarse-grained matrix of some TUBAF peridotites in this study are unlikely to exert a significant control on their bulk-rock compositions (Fig. 2a). This is inferred by the very low calculated contents in this mineral (≤0.7 ± 0.3 wt%; Table S1), which are consistent with the

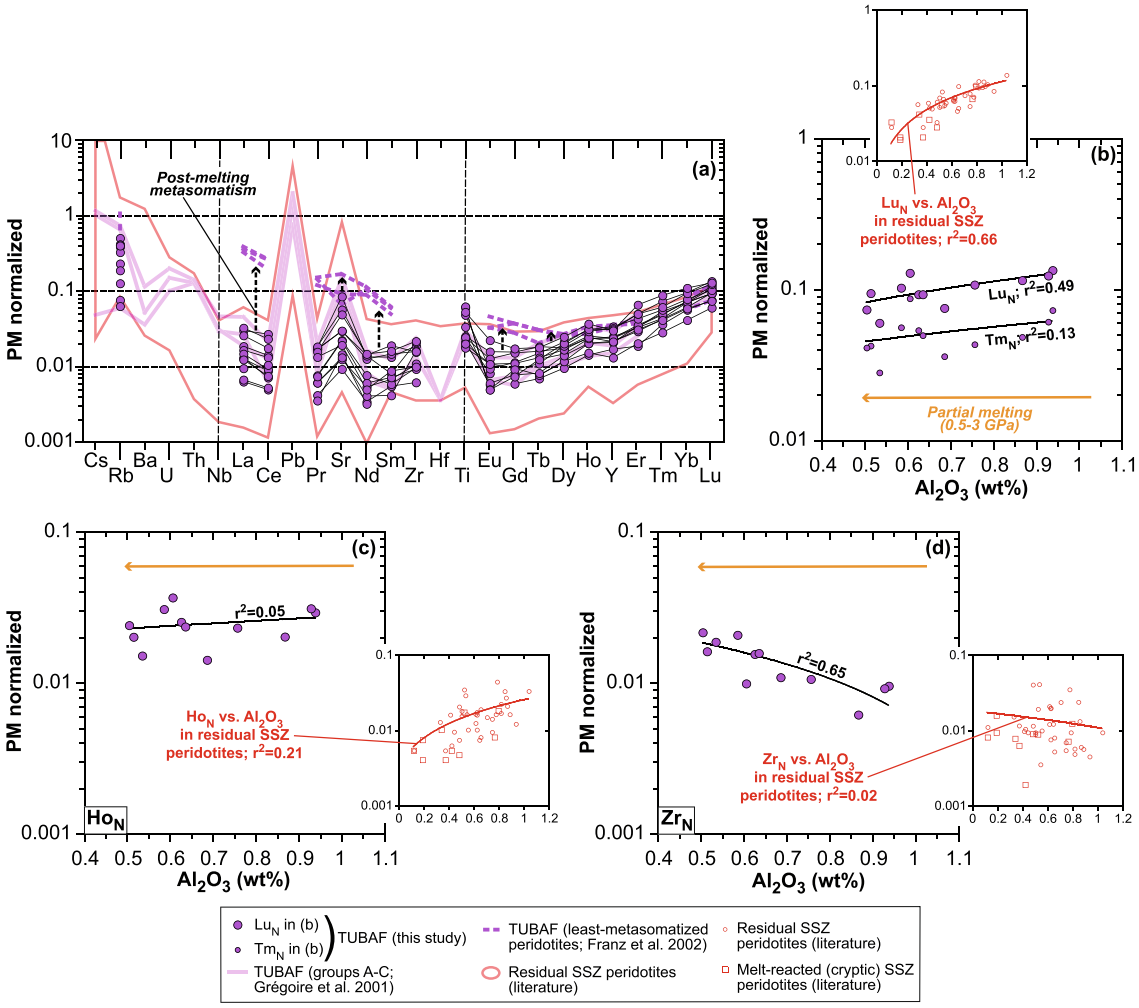

Fig. 7. Trace element abundances in bulk TUBAF peridotites in this study. (a) Primitive mantle-normalized trace element patterns and (b–d) co-variation plots of primitive mantle-normalized trace element abundances (subscript 'N') versus Al_2O_3 contents (in wt%) in bulk rocks. Primitive mantle data are from McDonough and Sun (1995). Also shown for comparison in (a) are data for residual TUBAF peridotites from Grégoire et al. (2001) referred to as groups A, B and C in the original publication (light pink patterns), the least-metasomatized TUBAF peridotites from Franz et al. (2002) (dotted pink patterns), and residual SSZ peridotites (red contour; Parkinson and Pearce, 1998; Ionov, 2010). The IBM samples 2R-1 and 3R-CC (Parkinson and Pearce, 1998) and the Kamchatka samples Av1 and Av16 (Ionov, 2010) are classified as 'melt-reacted (cryptic) SSZ peridotites' here. All trends are linear with a correlation coefficient (r^2) is given for each trace element considered in (b–d). Other symbols and acronyms are as in Figs. 2–6. (For interpretation of the references to colour in this figure legend, the reader is referred to the web version of this article.)

highly (TiO_2, Na_2O, K_2O)-depleted bulk-rock compositions, whether samples contain Mg-hornblende or not (Fig. 5d and f and Tables 1 and 2). Selective bulk-rock enrichments in some highly incompatible trace elements could be influenced by post-melting addition of Mg-hornblende (e.g. Ba and Rb; Figs. 7a and S10). However, this interpretation is unlikely for U-shaped REE patterns as (i) some amphibole-free samples are as enriched in LREE as those containing this mineral (e.g. sample 136310-1Q; Tables 1 and 5); and (ii), Mg-hornblende displays REE patterns parallel to neighbouring coarse cpx (Fig. S10).

In order to constrain further the respective controls of the coarse-grained matrix, disseminated amphibole and intergranular material on trace elements in bulk TUBAF peridotites, we have calculated their abundances on the basis of mineral and modal compositions (Figs. 10a and S12 and Table 6). Results show that, if there is a good agreement between calculated and measured bulk rocks for elements less incompatible than Dy (i.e. HREE; Figs. 10a and b and S12), others are systematically enriched in the measured ones (e.g. by a factor of up to 10 for elements as incompatible as LREE or more; Figs. 10c–e and S12). In the cases of MREE and LREE, however, it is clear that this level of enrichment cannot result from the presence of disseminated Mg-hornblende. For instance, introducing the composition of this mineral in the bulk-rock calculation of sample 136310-1AB triggers an enrichment factor of $\leq$1.5 for most trace elements, with the exception of Pb, Ba and Rb (1.7–2.0; Table 6). We conclude that the

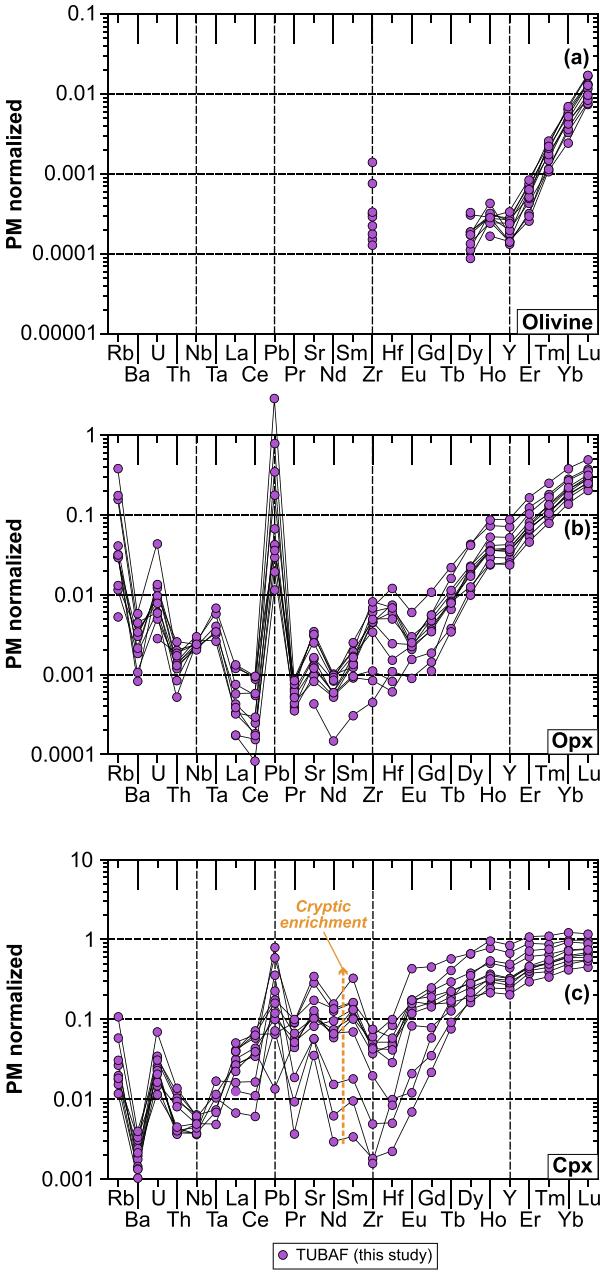

Fig. 8. Primitive mantle-normalized trace element patterns of average coarse (a) olivine, (b) opx and (c) cpx in TUBAF peridotites in this study. Primitive mantle data are from McDonough and Sun (1995). Symbols and acronyms are as in Figs. 2–7.

enrichment in all elements more incompatible than Dy in the measured bulk rocks is related to intergranular material rather than disseminated amphibole (Figs. 10 and S12). Below, we only consider the calculated trace element abundances in bulk TUBAF peridotites for our discussion.

Fine-grained pockets in TUBAF peridotites in this study partially replace coarse cpx, and appear intimately associated with the presence of Mg-hornblende relics, i.e. the most fusible mineral in these rocks (Figs. 2a, S4 and S5). The acicular texture and intra-crystal chemical zoning of pyroxenes, as well as the presence of glass, in the fine-grained pockets indicate the involvement of a silicate melt phase and high cooling rates (Figs. 2a, S4 and S5; Shea and Hammer, 2013), but there is no evidence for melt or fluid transfer through the xenoliths to the fine-grained pockets. Fine-grained opx and cpx in the pockets are close in composition to their coarse-grained counterparts, though typically more refractory (e.g. higher Cr_2O_3 contents or Mg#), with some evidence for local equilibrium with Mg-hornblende (Fig. S9). Importantly, LA-ICP-MS analyses of the bulk fine-grained pockets (opx + cpx + glass aggregates) indicate that they contain ~12 wt% CaO, i.e. as disseminated Mg-hornblende (Tables S7 and S21), and their trace element patterns largely mimic those of former coarse cpx or disseminated Mg-hornblende (Figs. 2a, S4, S5 and S10).

Taken together, textural and geochemical data on the fine-grained pockets are consistent with those in earlier studies documenting incongruent melting processes affecting a given mineral in xenoliths (Carpenter et al., 2002; Shaw and Klügel, 2002; Shaw, 2009; Pan et al., 2018), but not with late-stage interactions between xenoliths and their carrier magmas, which produce sieve texture in different phases simultaneously (Shaw and Klügel, 2002; Shaw et al., 2006; Shaw and Dingwell, 2008). We conclude that fine-grained pockets result from incongruent melting of disseminated Mg-hornblende, which formed earlier by the partial replacement of coarse cpx. Considering quenching textures of the fine-grained pockets, Mg-hornblende melting was likely driven by decompression during the upward entrainment of the xenoliths in their carrier magmas. In line with the lack of systematic variation in major or trace element compositions of bulk TUBAF peridotites with the occurrence of Mg-hornblende and fine-grained pockets (Tables 1 and S1), trace element analyses suggest that their formation occurred in a nearly isochemical system (Fig. S10).

Overall, bulk-rock and mineral compositions of the peridotites in this study display no or very limited Cr_2O_3-MnO-NiO and TiO_2-Na_2O-Mg# variations typical of either modal or cryptic post-melting metasomatism observed in some SSZ peridotites, including those previously reported from TUBAF (Figs. 4 and 11a–f; Pearce et al., 2000; McInnes et al., 2001; Franz et al., 2002; Franz and Romer, 2010; Bénard et al., 2017a). We conclude that the TUBAF peridotites in this study have suffered little post-melting modifications.

6.2. TUBAF peridotites in this study as pristine melting residues: High-temperature signatures preserved through subsolidus cooling and inter-mineral chemical equilibration

High-temperature signatures are well documented by the mineralogy, and bulk-rock and mineral compositions of TUBAF peridotites in this study. Large degrees of melting (≥25%) are notably indicated by low cpx contents, and the strong depletions in TiO_2, Al_2O_3, alkali oxides, HREE and MREE, which contrast with the elevated MgO, Mg# and Cr# characterizing bulk-rock and mineral compositions (Figs. 3–6, 8 and 10a). However, the final equilibration con-

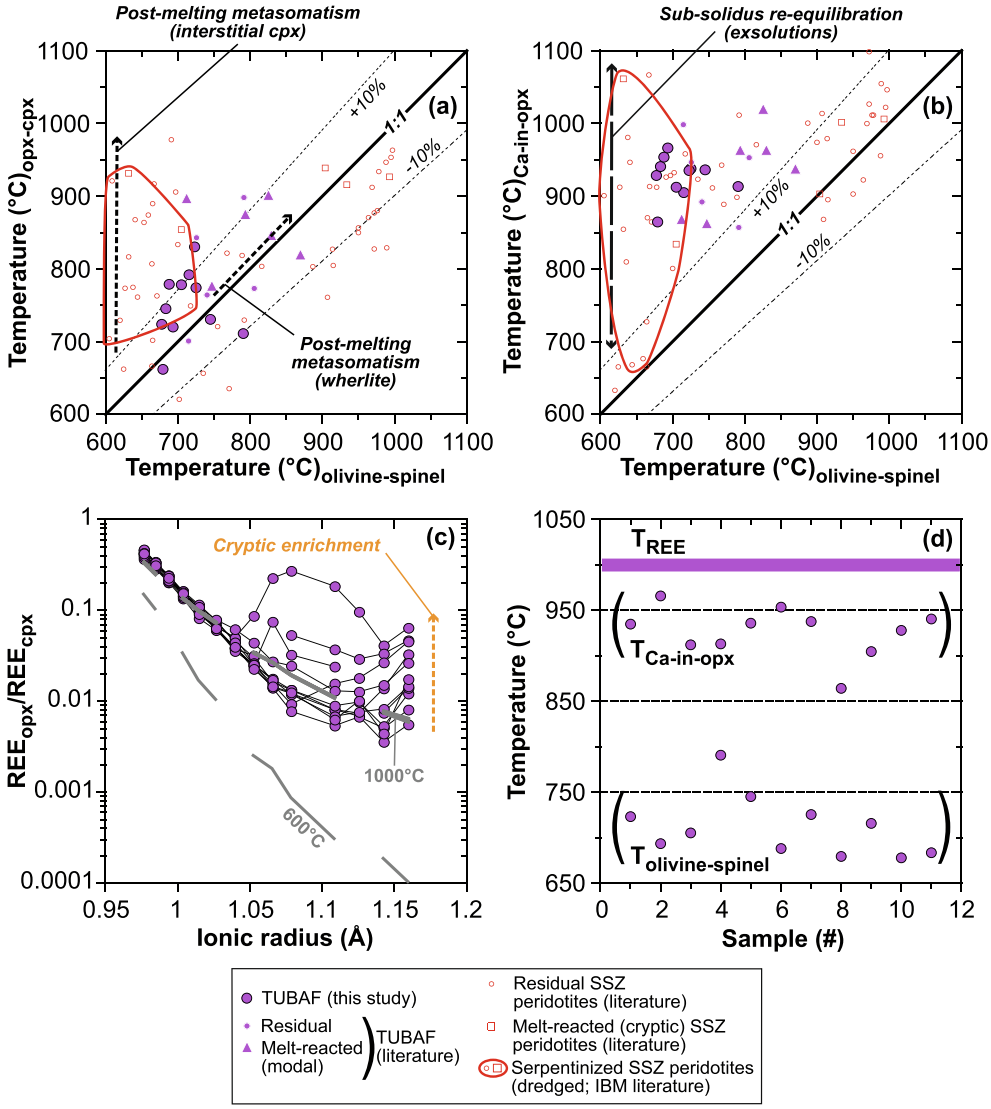

Fig. 9. Equilibration temperatures (in °C) of TUBAF peridotites in this study estimated using various methods. Co-variation plots of (a) opx-cpx and (b) Ca-in-opx versus olivine-spinel temperatures calculated using the geothermometers of Brey and Köhler (1990) and Ballhaus et al. (1991), respectively (c) Calculated partitioning coefficients between average coarse opx and cpx for rare-earth elements (REE) versus their VIII-fold ionic radii (Shannon, 1976), compared with models calculated at 600 °C (thin) and 1000 °C (bold) using the parameterization of Witt-Eickschen and O'Neill (2005) (grey lines). (d) Spectrum of all equilibration temperatures calculated with the different methods. T, temperature. Other symbols and acronyms are as in Figs. 2–7.

ditions of TUBAF peridotites range from ~1000 °C down to ~700 °C, depending on the blocking temperatures of the different systems (e.g. REE versus Fe-Mg inter-mineral diffusion; Fig. 9d), which reveal pronounced cooling to sub-solidus conditions experienced in the mantle lithosphere. The succession of high-temperature melting and long-term cooling is also consistent with the presence of exsolutions in all coarse pyroxenes, regardless of the grain morphology (Figs. 2, S4 and S5).

Despite sub-solidus cooling, TUBAF peridotites in this study have well-equilibrated coarse minerals, which preserve the original signatures of high-temperature melting. TUBAF peridotites notably display a wide range in spinel Cr# (Fig. 6f), which has been viewed as a potential proxy for the extent of melting in mantle rocks (Arai, 1994; Hellebrand et al., 2001). However, spinel Cr# may also be affected by the pressure-temperature (P-T) conditions of melting (Fig. 6f; Arai, 1994; Doucet et al., 2012), and those of sub-solidus re-equilibration (Ionov, 2010; Voigt and von der Handt, 2011). A slight positive correlation of spinel Cr# with the calculated opx-cpx temperatures of residual SSZ peridotites worldwide suggests that sub-solidus re-equilibration may play a role on a global scale, but no correlation is observed for TUBAF peridotites alone (Fig. 12a). Given that the bulk compositions of these rocks follow the 25–30% melting isopleths from ~2 to <1 GPa (Fig. 5a), a pressure effect on spinel Cr# could be visible. Indeed, most samples define a positive correlation between

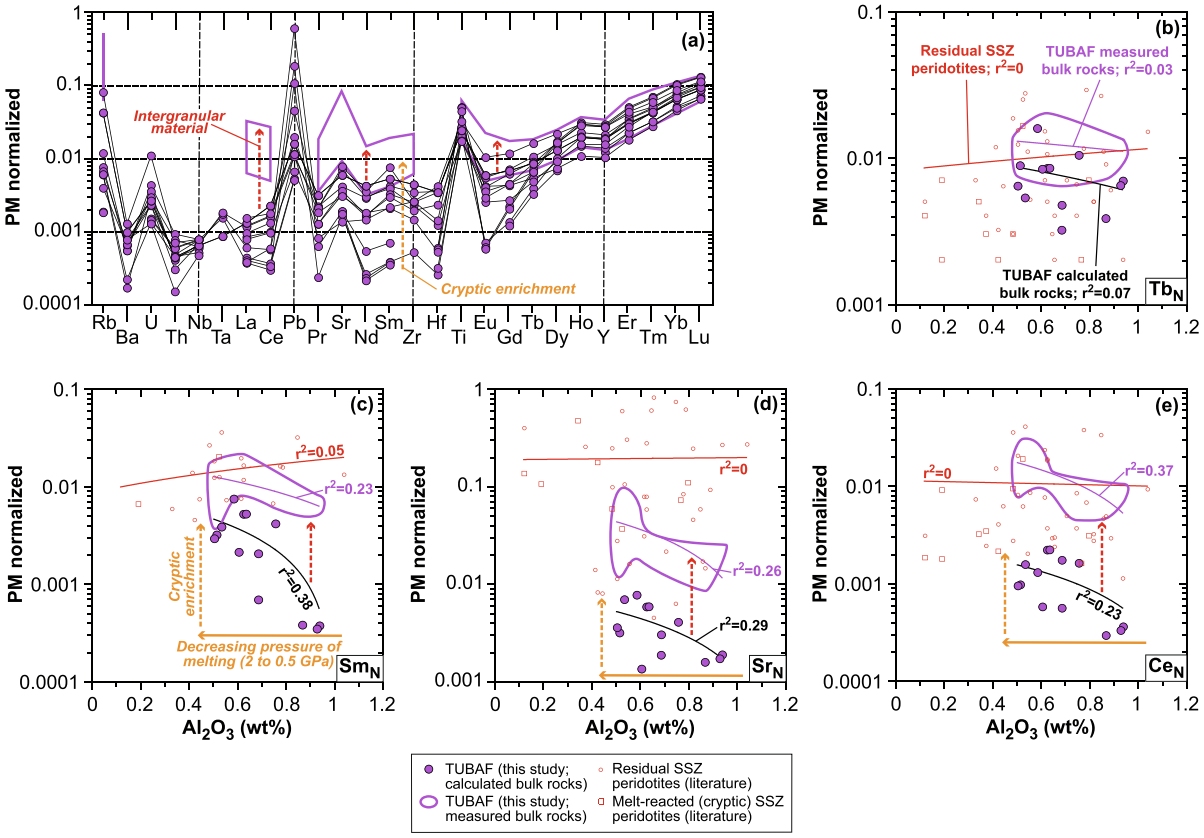

Fig. 10. Trace element abundances in bulk TUBAF peridotites in this study calculated from average coarse mineral and modal compositions. (a) Primitive mantle-normalized trace element patterns and (b–e) co-variation plots of primitive mantle-normalized trace element abundances versus Al_2O_3 contents (in wt%) in bulk rocks. Primitive mantle data are from McDonough and Sun (1995). Also shown for comparison are the measured trace element abundances in bulk rocks in this study (pink contour). All correlation trends are linear. Other symbols and acronyms are as in Figs. 2–9. (For interpretation of the references to colour in this figure legend, the reader is referred to the web version of this article.)

spinel Cr# and bulk FeO_t contents, which slope is similar to the one reported for residual cratonic peridotites (Fig. 12b; Doucet et al., 2012). We note, however, that samples with bulk-rock FeO_t contents suggesting melting at <1 GPa (i.e. in the plagioclase stability field; Walter et al., 1995) do not follow this trend, likely because spinel is of sub-solidus origin at these conditions (Fig. 12b). Taking two extreme cases along the trend (samples 136309-1B and 136309-1D; Fig. 12c), it appears that spinel with the highest Cr# coexists with pyroxenes containing the highest Cr_2O_3 for a given Al_2O_3 (Fig. 12d and e). This suggests Al-Cr equilibration conditions between the different minerals, which is confirmed for the whole sample suite by a positive correlation between pyroxene and spinel Cr# (Fig. 12f).

Spinel Cr# further correlates negatively with the bulk Al_2O_3 contents of TUBAF peridotites, which is a compositional parameter that has also been viewed as a solid indicator of the melt-depletion degree of SSZ mantle rocks (Fig. 13a; Ionov, 2010). In the case of TUBAF peridotites, however, the bulk Al_2O_3 content is a primary reflection of the evolution of the 25–30% melting isopleths with decreasing pressure, as they describe negative slopes in an FeO_t versus Al_2O_3 space (Fig. 5a). As a direct consequence of the good inter-mineral equilibration conditions outlined previously, the bulk Al_2O_3 contents further correlate negatively with pyroxene Cr# (Figs. 12f and 13b). Consistency between mineral and bulk-rock compositions of TUBAF peridotites is also apparent when considering Mg#, though the relationships remain weaker for samples which bulk-rock FeO_t contents suggest melting at <1 GPa (Fig. 13c). Negative correlations are observed between primitive mantle-normalized abundances of the moderately incompatible HREE to MREE in coarse cpx and spinel Cr#, allowing us to extend the approach of Hellebrand et al. (2001) to higher melting degrees than typically observed for abyssal peridotites (Fig. 13d). In the case of TUBAF peridotites, this trend in minerals fits well with the progressive extraction of the same moderately incompatible trace elements from a decompressing mantle, as previously inferred from positive correlations of their abundances with bulk Al_2O_3 contents (Figs. 7b and S12). In particular, the lower HREE abundances in the samples that experienced melt extraction at shallower depths (i.e. as indicated by higher spinel Cr#; Fig. 13d) must be related to changes in the melting reactions with decreasing pressure, such as those controlled by the increasing stability of olivine at the expense of pyroxenes in residues (e.g. Walter et al., 1995).

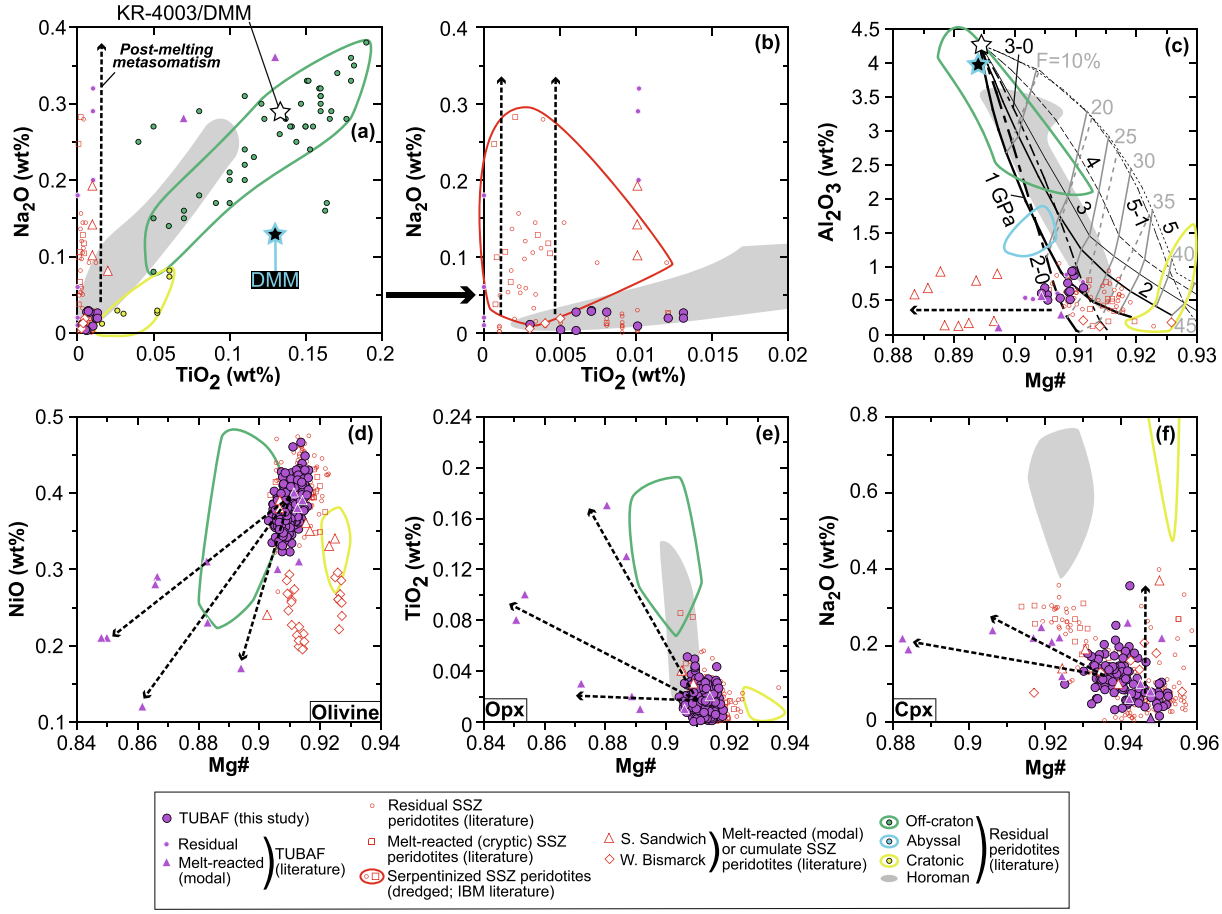

Fig. 11. Co-variation plots of major element oxide compositions (in wt%) and Mg# of (a–c) bulk TUBAF peridotites in this study and (d–f) their coarse minerals. Trends for the melting residues of KR-4003 lherzolite (Walter, 1998) in (c), as reported in Herzberg (2004), are also shown in Fig. 5. Other symbols and acronyms are as in Figs. 2–9.

We conclude that mineral and bulk-rock compositional trends for TUBAF peridotites in this study are fully coupled and consistent with the preservation of high-temperature melting signatures in these rocks. These signatures are primarily controlled by the polybaric evolution of residues along the 25–30% melting isopleths.

6.3. A re-assessment of earlier studies: The origins of TUBAF peridotites and the 'residual SSZ signatures'

Though earlier reports of TUBAF peridotites have largely concentrated on post-melting metasomatic processes, McInnes et al. (2001), Grégoire et al. (2001) and Franz et al. (2002) have also reported data on samples for which a residual origin is very likely, as their mineral and bulk-rock compositions and temperatures of equilibration are consistent with those in this study (Figs. 3–6, 7a, 9, 11, 12a, b and f and S8). Exceptions to this general tendency, however, include the sometimes-higher bulk-rock Na_2O, K_2O and highly incompatible trace element contents of samples in these earlier studies compared to ours, which likely point to a greater influence of post-melting metasomatic processes (Figs. 5f, 7a and 11a and b). Based on spinel Cr#-Mg# and coarse cpx trace element compositions, as well as slow cooling rates inferred from spinel exsolutions and intra-crystal chemical zoning of olivine, it was argued that TUBAF peridotites originally formed by melting at a mid-ocean ridge (McInnes et al., 2001; Grégoire et al., 2001; Franz et al., 2002).

In the light of our new data and the compiled compositional ranges of residual peridotites from various tectonic settings, a mid-ocean ridge origin for TUBAF peridotites appears unlikely. This is notably indicated by the higher degree of melting these samples record (≥25%) in comparison with abyssal peridotites (≤20%; Figs. 4, 5a–e and 11c). Higher melting degrees are also derived from the relationships between trace element abundances in coarse cpx and spinel Cr#, which is a valid proxy when comparing rocks formed on a similar pressure range of melting (Figs. 5a and 13d; Hellebrand et al., 2001). We note that larger bulk-rock datasets for abyssal peridotites still indicate that these rocks predominantly form by ~20% melting at ≤2 GPa (e.g. n = 446; Doucet et al., 2012). Large datasets also support that no cpx in abyssal peridotite record $Lu_N \leq 1$ as in TUBAF samples (Fig. 8c), keeping in mind that the sub-solidus temperature effect on opx-cpx trace element redistribution must be similar for all these rocks. However, there is an overlap in spinel Cr# between TUBAF and

Table 6
Calculated bulk-rock trace element abundances (ppm. except where noted).

Sample	136309-1AA	136309-1B	136309-1C	136309-1D	136309-1E	136310-1AB	136310-1AB[a]	136310-1AB[a,b]	136310-1AO	136310-1AT	136310-1F	136310-1Q	136310-1Z	136310-1Z[a]
CaO (wt%)	1.04	1.12	0.80	0.69	0.68	0.88	0.89	0.88	0.74	0.46	0.64	0.78	0.93	0.86
Sc[c]	12	13	8.81	12	11	12	12	13	11	8.28	9.68	9.54	11	10
Ti[d]	29	24	21	21	33	29	29	28	29	53	38	21	60	59
V	46	52	34	48	38	43	44	44	42	28	42	38	48	48
Cr[d]	2959	3090	2754	4043	3523	3387	3400	3241	3340	2446	3346	3289	3648	3663
Mn[d]	1009	991	945	1007	1042	1035	1035	1031	1031	1045	1049	1061	955	956
Co	119	113	121	120	121	118	118	118	124	131	129	129	119	119
Ni	2461	2347	2590	2489	2443	2396	2391	2396	2469	2551	2577	2569	2424	2434
Zn	46	47	49	57	55	53	53	52	60	57	61	58	63	63
Rb	0.0070	0.0024	–	0.0045	0.0040	0.025	0.025	0.042	0.048	–	0.0036	0.0036	0.0011	0.0011
Sr	0.081	0.031	0.037	0.138	0.063	0.117	0.117	0.138	0.060	0.027	0.154	0.071	0.038	0.034
Y	0.090	0.077	0.052	0.044	0.081	0.078	0.078	0.107	0.067	0.115	0.114	0.059	0.125	0.119
Zr	0.036	0.0054	–	0.024	0.026	0.046	0.046	0.059	0.015	0.027	0.027	0.020	–	–
Nb	0.0006	0.0005	0.0005	0.0006	0.0005	0.0005	0.0005	0.0007	0.0006	0.0006	–	0.0004	0.0006	0.0005
Ba	0.0036	0.0043	0.0051	0.0036	0.0044	0.0064	0.0064	0.013	0.0084	0.0051	0.0011	0.0015	–	–
La	0.0008	0.0002	0.0004	0.0007	0.0005	0.0008	0.0008	0.0013	0.0010	0.0002	0.0006	0.0005	0.0003	0.0003
Ce	0.0027	0.0005	0.0009	0.0027	0.0016	0.0037	0.0037	0.0054	0.0029	0.0010	0.0022	0.0016	0.0006	0.0006
Pr	0.0006	0.00006	0.0002	0.0005	0.0003	0.0008	0.0008	0.0011	0.0005	0.0002	0.0005	0.0003	–	–
Nd	0.0036	0.0003	0.0007	0.0037	0.0020	0.0052	0.0052	0.0075	0.0022	0.0018	0.0044	0.0021	0.0003	0.0003
Sm	0.0017	0.0002	0.0003	0.0016	0.0013	0.0021	0.0021	0.0031	0.0008	0.0009	0.0030	0.0012	0.0002	0.00014
Eu	0.0008	0.0001	–	0.0006	0.0006	0.0009	0.0009	0.0013	0.0004	0.0004	0.0016	0.0005	0.00009	0.00009
Gd	0.0038	0.0007	0.0006	0.0023	0.0033	0.0037	0.0037	0.0053	0.0014	0.0024	0.0063	0.0024	0.0012	0.0011
Tb	0.0010	0.0004	0.0003	0.0005	0.0009	0.0008	0.0008	0.0012	0.0005	0.0008	0.0016	0.0006	0.0007	0.0006
Dy	0.010	0.0067	0.0046	0.0049	–	0.0086	0.0086	0.012	0.0061	0.011	0.014	–	0.011	0.011
Ho	0.0033	0.0029	–	0.0016	0.0030	0.0029	0.0029	0.0039	0.0023	0.0042	0.0044	0.0022	0.0046	0.0044
Er	0.015	0.015	0.0097	0.0078	0.013	0.013	0.013	0.017	0.012	0.019	0.018	0.0097	0.022	0.021
Tm	0.0032	0.0033	0.0022	0.0019	0.0029	0.0028	0.0029	0.0035	0.0029	0.0040	0.0034	0.0022	0.0047	0.0045
Yb	0.032	0.035	0.023	0.020	0.028	0.028	0.028	0.033	0.030	0.038	0.032	0.022	0.045	0.044
Lu	0.0068	0.0074	0.0048	0.0044	0.0058	0.0058	0.0058	0.0067	0.0063	0.0075	0.0063	0.0044	0.0088	0.0086
Hf	0.0010	0.00007	0.00009	0.0003	0.0010	0.0010	0.0010	0.0012	0.00015	0.0004	0.0012	0.0007	0.0002	0.0002
Ta	–	0.00006	0.00006	0.00007	–	0.00003	0.00003	0.00005	–	–	–	–	–	–
Pb	0.0016	0.016	0.027	0.0067	0.090	0.0023	0.0024	0.0041	0.0017	0.0017	0.0029	0.0010	0.0008	0.0008
Th	0.00007	0.00004	0.00002	0.00003	0.00006	0.00004	0.00004	0.00004	0.00006	0.000012	0.00003	0.00004	0.00005	0.00005
U	0.00009	0.00005	0.00005	0.00007	0.00006	0.00005	0.00005	0.00006	0.0002	0.00003	0.00006	0.00003	0.00003	0.00003

[a] Using the modal composition of the duplicate analysis.
[b] Amphibole is included.
[c] Spinel is not included.
[d] Using EPMA data for pyroxenes and Cr in spinel.

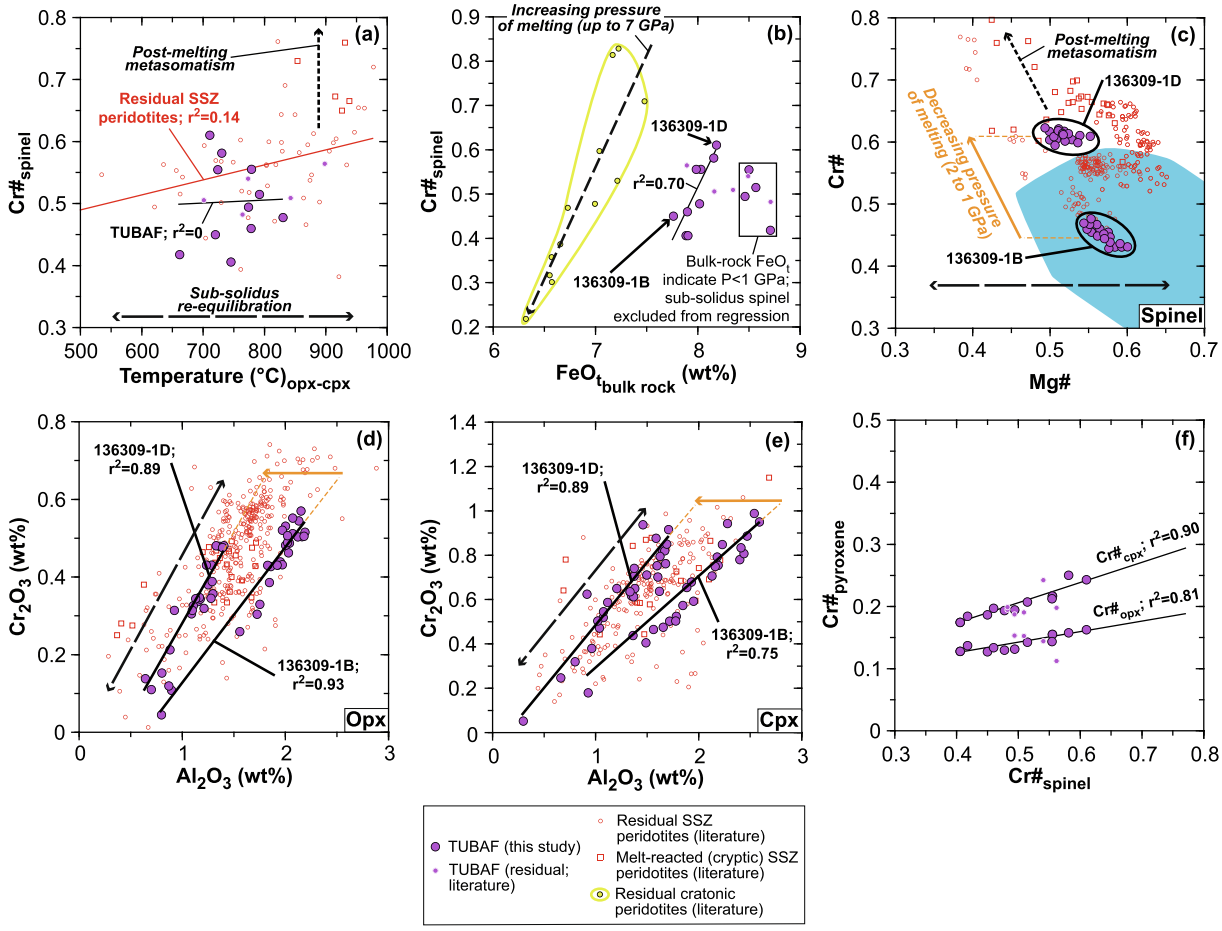

Fig. 12. Controls on spinel composition and spinel-pyroxene equilibration in TUBAF peridotites in this study. (a, b) Co-variation plots of average spinel Cr# versus (a) opx-cpx temperatures (calculated with the geothermometer of Brey and Köhler, 1990) and (b) bulk FeO_t contents (in wt%). (c–e) Co-variation plots of coarse mineral major element oxide compositions (in wt%), Mg# and Cr# for samples 136310-1B and 136310-1D (end-members in spinel Cr#). (f) Co-variation plot of Cr# of pyroxenes versus spinel (averages). Also shown in (c) for comparison are data for abyssal spinel peridotites of residual origin (light-blue field; Dick and Bullen, 1984; Niu and Hékinian, 1997; Warren, 2016). Literature data for TUBAF peridotites are not included in the correlations in this figure. All correlation trends are linear. Symbols and acronyms are as in Figs. 2–9. (For interpretation of the references to colour in this figure legend, the reader is referred to the web version of this article.)

abyssal peridotites ($0.1 \leq Cr\# \leq 0.6$; Figs. 6f and 12c; Dick and Bullen, 1984; Niu and Hékinian, 1997; Warren, 2016). Spinel $Cr\# \geq 0.5$ in abyssal peridotites has been mainly related to higher melting degrees at fast spreading rates (Niu and Hékinian, 1997) or the inheritance of highly-depleted sections in the oceanic mantle (Müntener and Manatschal, 2006). In the light of our results, however, the wide range in spinel Cr# of abyssal peridotites could be also originally controlled by polybaric melting (Fig. 5a; Stephens, 1997), though the formation of sub-solidus spinel after melting in the plagioclase stability field or post-melting metasomatism might also have affected this parameter (Figs. 12a–c and 13b and c). Finally, long-term and slow cooling in peridotites (i.e. in the order of several tens of Myrs at $\leq 20\ °C.Ma^{-1}$) is not limited to mid-ocean ridges, since such a process has been evidenced in residual SSZ peridotites worldwide (Parkinson and Pearce, 1998; Ionov, 2010; Soustelle et al., 2010, 2013; Bénard et al., 2017a; Tollan et al., 2017). Overall, TUBAF xenoliths display the distinctive silica enrichment of residual SSZ peridotites, whereas it is not the case for calculated bulk abyssal peridotites (i.e. from mineral and modal compositions; Baker and Beckett, 1999). We note that these bulk-rock calculations are critical to address the case of serpentinized peridotites, in particular their bulk silica contents (Malvoisin, 2015). Therefore, we re-assess earlier interpretations of the high-temperature melting origins of TUBAF peridotites at mid-ocean ridges (McInnes et al., 2001; Grégoire et al., 2001; Franz et al., 2002), as these rocks bear all the typical features of a SSZ environment.

The combination of the silica-enrichment and Fe-Al trends in the bulk compositions of TUBAF peridotites is a strong argument in favour of a residual origin for these rocks (Fig. 5a–c). The Fe-Al correlations record melting-degree isopleths and are predicted to occur in the residues of polybaric mantle melting (Herzberg, 2004). These correlations are rarely documented in mantle peridotites worldwide; they are unlikely to form by, or resist post-melting

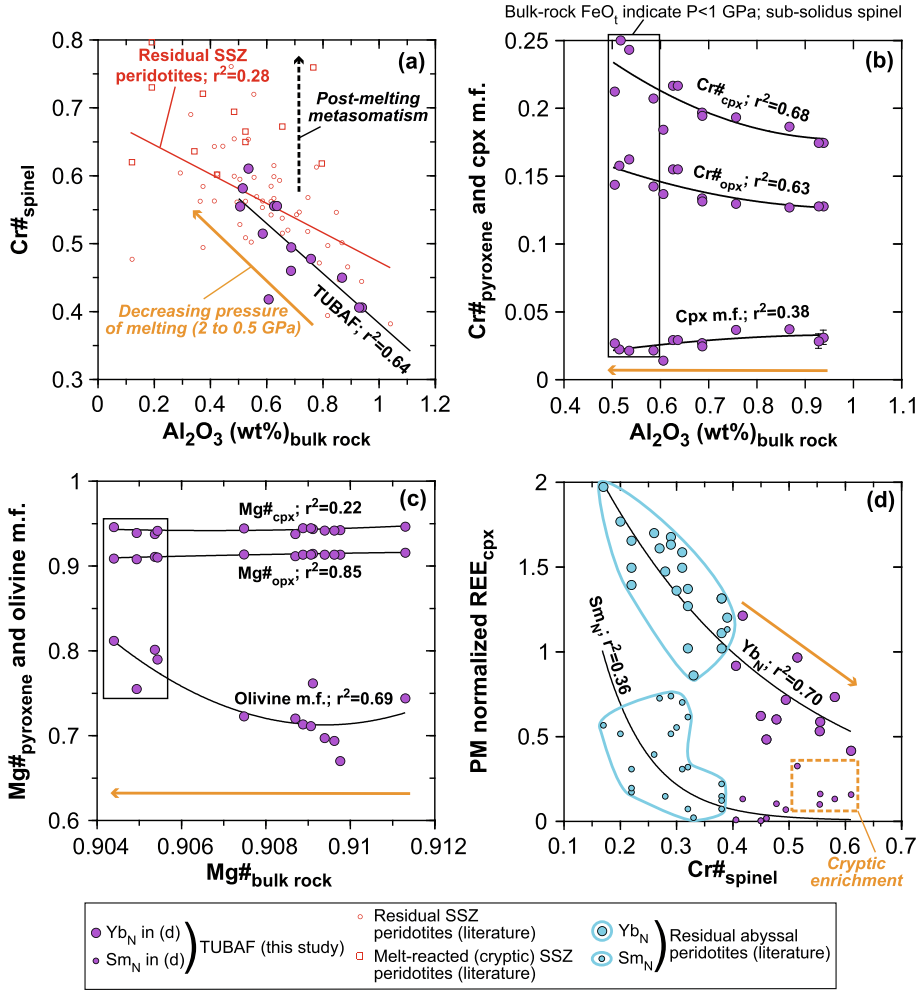

Fig. 13. (a–c) Co-variation plots of Mg#, Cr# and mass fraction (m.f.) of coarse minerals (averages) in TUBAF peridotites in this study versus their bulk major element oxide compositions (in wt%). (d) Co-variation plot of primitive mantle-normalized REE abundances in coarse cpx versus spinel Cr# (averages). Primitive mantle data are from McDonough and Sun (1995). The correlation trend in (a) is linear. Second-order polynomial correlation trends are used in (b) and (c), while those in (d) are exponential. P, pressure. Other symbols and acronyms are as in Figs. 2–9.

metasomatism such as Fe enrichment, which can occur in some SSZ peridotites (Fig. 11c) and similar rocks from other tectonic settings (e.g. Ionov et al., 2005). In fact, TUBAF seamount is only the fifth locality on Earth where a Fe-Al correlation is recognized in residual mantle peridotites, and the first in a SSZ environment (Stephens, 1997; Takazawa et al., 1996, 2000; Ionov, 2004, 2007; Ionov and Hofmann, 2007; Doucet et al., 2012). The clear relationships between SiO_2 and both Al_2O_3 and FeO_t contents (but also MgO) in bulk rocks (Fig. 5a–c), which in turn correlate with mineral compositions, further support the high-temperature melting origin of the silica enrichment in TUBAF peridotites, and by extension, in other residual SSZ peridotites.

In addition to their silica-enriched nature, TUBAF and other residual SSZ peridotites tend to be more depleted in incompatible element oxides (TiO_2, Al_2O_3 and Na_2O) for a given MgO content than residues of fertile mantle melting (Fig. 5d–f; Ionov, 2004, 2007; Ionov and Hofmann, 2007). These two key compositional features make residual SSZ peridotites unique among those from other tectonic settings; we define them here as ‘residual SSZ signatures’. When compared to KR-4003 residues (Herzberg, 2004), we note that the degree of silica enrichment of residual SSZ peridotites (by up to ~2 wt% SiO_2; Fig. 5b) is not directly counterbalanced by the degree of their Al_2O_3 depletion (by up to ~0.5 wt%; Fig. 5e), so that further addition of excess silica is required. This is in line with high opx contents near cpx-out conditions in some residual SSZ peridotites (Figs. 3 and S6).

In his seminal study, Herzberg (2004) stated that SSZ peridotites are generally ‘too enriched in SiO_2 and too depleted in Al_2O_3 to be melting residues’. On the contrary, we argue that TUBAF and other SSZ peridotites, despite showing these typical enrichments in silica and depletions in Al_2O_3 (together with TiO_2 and Na_2O), display all the signatures of mantle melting residues. The fact that residual SSZ peridotites are relatively depleted in incompatible ele-

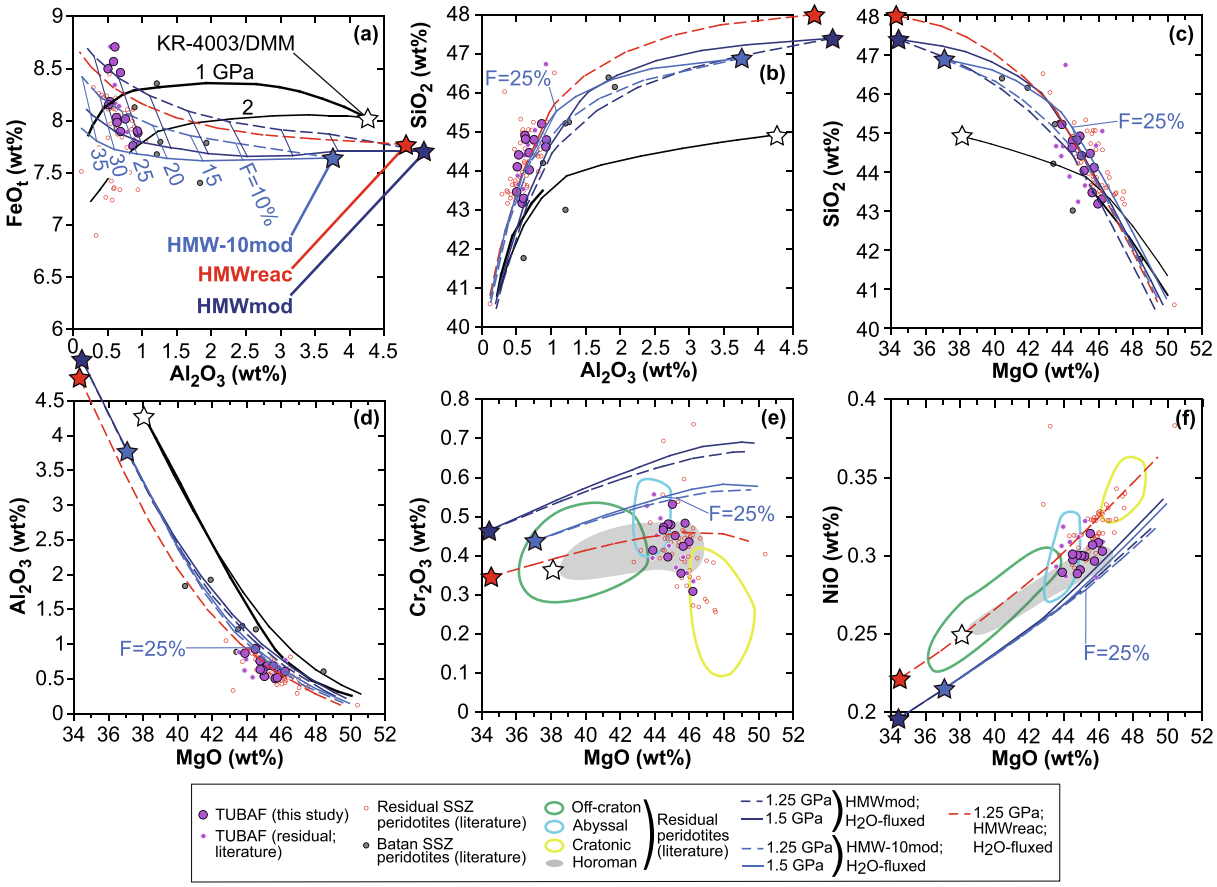

Fig. 14. Co-variation plots of major element oxide compositions (in wt%) of bulk TUBAF peridotites, compared with the melting models in this study. Models at 1.25 GPa are shown with dashed lines, while those at 1.5 GPa are shown with continuous lines. The flux-melting models of the hybrid mantle wedge (HMW) and pre-depleted HMW sources ('HMWmod' and 'HMW-10mod', respectively), both calculated on the basis of modal addition of opx to off-craton continental peridotites (Ionov, 2004, 2007; Ionov and Hofmann, 2007), are shown in dark blue and blue, respectively. The flux-melting model of the HMW source calculated by reaction (isenthalpic assimilation using pMELTS, Ghiorso et al., 2002) of 8% of a eclogite-derived melt (Kessel et al., 2005) with PM (Palme and O'Neill, 2014) is shown in red ('HMWreac'). Other symbols and acronyms are as in Figs. 2–13. (For interpretation of the references to colour in this figure legend, the reader is referred to the web version of this article.)

ment oxides could be inherited from melting processes or their pre-subduction history, for instance the 'pre-depleted' nature (i.e. in comparison with PM or even DMM) of peridotite protoliths convecting into the mantle wedge before it is modified by subduction components. This interpretation is in line with the fact that the TiO_2 and Na_2O compositions of residual SSZ peridotites agree well with trends defined by spinel-bearing rocks from the Horoman massif, which originate from a depleted source (i.e. containing $\leq$0.1 wt% TiO_2, $\leq$3.5 wt% Al_2O_3 and $\leq$0.3 wt % Na_2O; Fig. 5d–f, 6c–e, 11 and S8). Alternatively, these depletions could originate from the nature of the melting processes forming residual SSZ peridotites (e.g. equilibrium versus fractional).

Based on results from IBM, Kamchatka and West Bismarck SSZ peridotites, it has been proposed that the silica enrichment in these samples was produced during the last melting event in the mantle wedge to form spinel harzburgite residues, later accreted to the SSZ mantle lithosphere (Bénard et al., 2017a). These authors also calculated melting trends of a model hybridized source (i.e. silica- and opx-rich, and referred to as 'hybrid mantle wedge'; HMW) to reproduce the residual SSZ signatures; we extend this hypothesis below by using new modeling approaches.

6.4. Concurrent silica enrichment and (TiO_2, Al_2O_3, Na_2O)-depletion ('residual SSZ signatures'): Polybaric flux-melting models of hybridized mantle

In order to further investigate the possible range of high-temperature processes that could lead to the formation of the residual SSZ signatures, we use a polybaric flux-melting modeling approach with the pMELTS software (Ghiorso et al., 2002). Apart from varying source compositions and melting conditions, the fundamental difference with the models in Bénard et al. (2017a) here is that we constrain the behaviour of minor elements (Ti, Cr, Mn, Ni and Na) with partitioning coefficients. Regarding olivine-melt equilibrium, fixed partitioning coefficients are used for Ti, Cr and Na (Table S23), while parameterizations against

temperature and melt composition are used for Mn and Ni (equations 4 and 7 in Wang and Gaetani, 2008). In most cases, olivine-melt values are propagated to pyroxenes and spinel, using inter-mineral partitioning coefficients calculated from the average mineral compositions of TUBAF peridotites in this study (Table S23).

First, we model anhydrous melting along thermal gradients, i.e. as in Bénard et al. (2017a), but at 1.25 and 1.5 GPa. Second, we perform several isothermal calculations where increasing melting degrees are triggered by progressively adding H_2O to the system, respectively at 1250 °C for 1.25 GPa and at 1300 °C for 1.5 GPa. All calculations are executed at FMQ + 0.7 in order to allow a direct comparison with the results of Bénard et al. (2017a); these fO_2 conditions match those recorded by many silica-rich, residual SSZ peridotites (Bénard et al., 2018a,b). Nevertheless, the effects of varying this parameter during melting remain minor for this type of models (Bénard et al., 2017a). This calculation procedure follows the general principles of flux-melting, as conceptualized from field measurements and parameterized in the related melting equations (Stolper and Newman, 1994; Eiler et al., 2000; Bénard et al., 2017b). The P-T conditions aim at simulating the thermal structure of the upper part of a mantle wedge in a mature, intra-oceanic arc (Syracuse et al., 2010).

We use several sources in the models to investigate the effects of various pre-depletion degrees and hybridization processes on the compositions of melting residues. The source compositions used include: (i) KR-4003 lherzolite (Walter, 1998) with TiO_2, Cr_2O_3, MnO, Na_2O, K_2O and NiO contents as in DMM (Salters and Stracke, 2004), referred to as 'KR-4003/DMM'; (ii) two HMW-like sources calculated by modal addition of opx to either fertile (PM-like) or depleted (by ~10% melting at ca. 1–2 GPa of PM) off-craton continental peridotites (Ionov, 2004, 2007; Ionov and Hofmann, 2007), referred to as 'HMWmod' and 'HMW-10mod', respectively; and (iii), a HMW-like source calculated by reaction (isenthalpic assimilation using pMELTS) of ~8% of a eclogite-derived liquid (Kessel et al., 2005) with PM (Palme and O'Neill, 2014), referred to as 'HMWreac' (Table S24).

Modeling results confirm that, under anhydrous conditions, pMELTS tends to slightly overestimate opx abundances in the residues in comparison with experiments (Bénard et al., 2017a; Kimura, 2017). However, these differences remain minor (the only exception being for the bulk FeO_t contents of the residues) for the conditions investigated here, and our new anhydrous KR-4003/DMM melting models compare well with the results of Herzberg (2004) (Fig. S13). The partitioning coefficients for minor elements in our new models also reproduce the TiO_2, Cr_2O_3, MnO, NiO and Na_2O abundances for given MgO contents of residual peridotites (Fig. S13). Fluxing the system with H_2O typically produces residues that are relatively enriched in FeO_t and depleted in SiO_2 for given Al_2O_3 or MgO contents, which results from the enhanced stabilization of olivine relative to opx (or preferential opx dissolution by incongruent melting to form olivine) under hydrous conditions (Figs. S6 and S13; Kushiro et al., 1968; Inoue, 1994; Hirose and Kawamoto, 1995; Gaetani and Grove, 1998). In this context, only the polybaric flux-melting models of the three HMW-like sources allow reproducing both Fe-Al correlations and the silica enrichment at $F \geq 25\%$ observed in TUBAF and other residual SSZ peridotites (Figs. 14a–c). In addition, using a pre-depleted mantle protolith (HMW-10mod) provides the best fits for the SSZ (TiO_2, Al_2O_3, Na_2O)-depletion trends (Fig. 14d). However, among the three hybridized sources, only the one calculated by reaction of peridotite with a eclogite-derived liquid (HMWreac) can explain the abundances of compatible (Cr and Ni) and slightly incompatible (Mn) elements in TUBAF and other residual SSZ peridotites (Fig. 14e and f).

To extend the modeling to REE, we perform non-modal melting models using (i) the KR-4003/DMM and HMWreac source modal compositions with REE abundances as in PM (McDonough and Sun, 1995); (ii) equilibrium (or batch) and fractional melting equations of Shaw (1970); (ii) dynamic melting equations of Zou (1998); (iii) melting reactions to reproduce the residue modal compositions obtained with pMELTS; and (iv), the mineral-melt partitioning coefficients of McDade et al. (2003a, b). Test calculations reveal that it is impossible to reproduce the calculated HREE-MREE patterns of bulk TUBAF peridotites by batch melting unless nearly all residual opx is consumed, on the contrary to fractional melting models (Fig. 15a and b). However, fractional melting models of the KR-4003/DMM source reveal inconsistencies with inferences from the Fe-Al correlation in TUBAF peridotites ($F \geq 25\%$; Fig. 5a), as the HREE-MREE abundances are rather reproduced for melting degrees ranging from ~20% to only slightly above (Fig. 15a). This is not the case for fractional melting models of the HMWreac source, which provide the best fit at F ~25% for the HREE-MREE abundances in the least HREE-depleted TUBAF peridotites (Fig. 15b). This reveals that sufficiently high opx abundances are left in the residues of a hybridized source to account for the HREE-MREE abundances in TUBAF peridotites at ≥25% melting, which is in line with the modeling results for major elements (Fig. 14b and c). Dynamic melting models confirm that the trace element compositions of TUBAF peridotites can only be reproduced if melt extraction occurs in a nearly-pure fractional mode (critical mass porosity <0.001%; Fig. 15c). Assuming a closed system, fractional and dynamic melting of the HMWreac source cannot reproduce the strong enrichments in MREE-LREE, which are notably observed in the most HREE-depleted TUBAF peridotites (F ~30%; Fig. 15b and c).

6.5. Implications for the nature of fractional hybridization-melting processes in the SSZ mantle and relationships with the present-day TLTF tectonic setting

In this study, we extend the hypothesis of Bénard et al. (2017a) and show that isothermal flux-melting of a HMW source produces the best fits of the residual SSZ signatures, with the requirement that this hybridized source results from the interaction of a silica-rich liquid with a pre-depleted peridotite protolith (Figs. 14 and 15b). This model for the formation of silica enrichment among other residual SSZ signatures is consistent with evidence from high-P

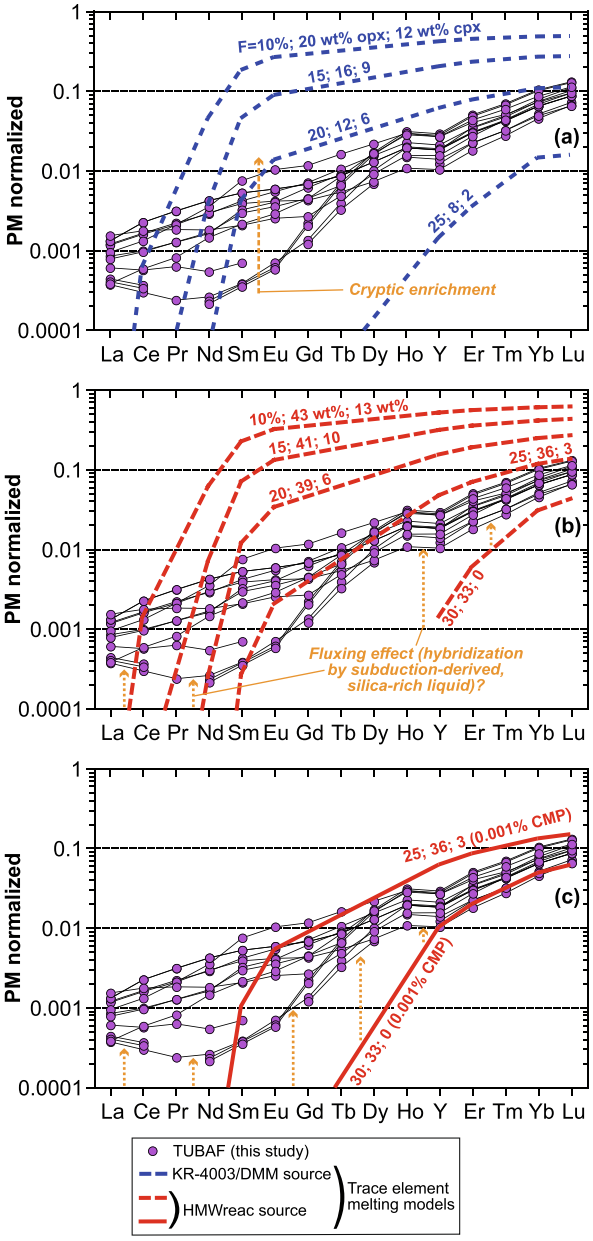

Fig. 15. Comparison between primitive mantle-normalized trace element patterns of calculated bulk TUBAF peridotites in this study and the results for fractional and dynamic flux-melting models. Fractional flux-melting models for (a) the KR-4003/DMM source (dashed dark-blue lines) and (b) a HMWreac source (dashed red lines). (c) Dynamic flux-melting model for a HMWreac source with a critical mass porosity (CMP) of 0.001% (continuous red lines). Primitive mantle data are from McDonough and Sun (1995). Both models use the same source compositions and similar melting reactions as those modelled at 1.25 GPa, which are shown with the same color code in Figs. 14 and S13. Other symbols and acronyms are as in Figs. 2–14. (For interpretation of the references to colour in this figure legend, the reader is referred to the web version of this article.)

experiments. Mantle-sediment or mantle-oceanic crust reaction experiments have outlined the development of opx-rich reactions zones (Yaxley and Green, 1998; Woodland et al., 2018), while experiments of mantle hybridization-melting involving subduction-derived liquids have reported the systematic presence of liquidus opx or opx-rich residues (Sekine and Wyllie, 1982; Johnston and Wyllie, 1989; Carroll and Wyllie, 1989; Rapp et al., 1999; Rapp et al., 2010; Mallik et al., 2015, 2016). This is because dehydration or melting of sediment and oceanic crust typically produces hydrous, silica-bearing liquids that can partially transform mantle olivine into opx (e.g. Kessel et al., 2005; Hermann and Spandler, 2008; Ionov et al., 2011; Bénard et al., 2018b). Despite the fact that rare SSZ peridotites contain $\geq$45.5 wt% SiO_2 (e.g. Batan xenoliths; Maury et al., 1992), most samples seem to range below this limit (Fig. 5b and c). This restricted compositional range could result from the particular solute compositions in the fluxing liquid, which would control both the extents of silica enrichment in residues and the melting degree at the same time (e.g. alkali aluminosilicate polymers in fluids versus silicate melts; Manning, 2004; Kessel et al., 2005; Hermann and Spandler, 2008). Discriminating such a single-stage process from melting of a solid HMW source, for instance originally formed at a slab-mantle wedge interface (e.g. Endo et al., 2015) and later recycled through diapirism (e.g. Behn et al., 2011), remains difficult at present and requires further studies.

Our model for the formation of (TiO_2, Al_2O_3, Na_2O)-depletion among the key residual SSZ signatures is consistent with well-established geochemical evidence for a greater melt-depletion degree of the mantle wedge sources of Western Pacific, intra-oceanic arc magmas, in comparison with those of mid-ocean ridge basalts (e.g. 'conservative' trace element abundances; Woodhead et al., 1993). Furthermore, it is also consistent with more recent evidence from Fe isotope systematics, since this geochemical proxy can be used in magmas to infer the melt-depletion degree of their mantle sources (e.g. Nebel et al., 2018). These studies have notably outlined that the δ^{57}Fe of Western Pacific, intra-oceanic arc magmas extend to very light values, reflecting mantle sources much more depleted than those of mid-ocean ridges and Eastern Pacific continental arcs (Nebel et al., 2015; Foden et al., 2018). These data are consistent with $\geq$10% melt extraction from PM for pre-subduction mantle protoliths, as we model for residual SSZ peridotites from Western Pacific arcs (Fig. 14b), and might be related to earlier melting events at intra-oceanic rifts before further convective recycling in the mantle wedge.

Our trace element models imply that hybridization-melting of the SSZ mantle is close to purely fractional. This observation is consistent with the fact that mantle melting seems to operate in a fractional mode globally, as evidenced from the REE patterns of mantle cpx at mid-ocean ridges (e.g. abyssal peridotites in Warren, 2016). However, no melting model assuming a closed system can reproduce the MREE-LREE-enriched calculated patterns of TUBAF peridotites (Fig. 15b). The abundances of highly incompatible trace elements correlate negatively with Al_2O_3 contents in bulk TUBAF peridotites (Figs. 10b–e and S12), which appear to be primarily controlled by MREE-LREE cryptic metasomatism in coarse cpx (Figs. 8c, 9c and 13d). For

instance, there are no relationships between these correlations and the extent of sub-solidus MREE-LREE disequilibrium between pyroxenes (Figs. 9c and S14). Therefore, these correlations rather suggest open-system melting triggered by the ingress of a mobile agent enriched in these elements, which could be directly related to the effects of hybridization (or fluxing) involving SSZ fluids or silicate melts. A similar, open-system process has been deduced in studies of ophiolitic fore-arc peridotites recording similar melt-depletion degrees as those from TUBAF (Pagé et al., 2009), and could be consistent with a single-stage process where hybridization and melting occur at the same time.

The Fe-Al correlation extends to relatively high FeO_t contents near 8.5 wt% in TUBAF peridotites. These relatively high FeO_t contents record decompression-driven melting to very shallow depths, which likely involves mantle adiabatic upwelling to <1 GPa, such as it can occur at mid-ocean ridges (Fig. 5a; Stephens, 1997). Very shallow melting conditions are also typical for intra-oceanic rifts in fore-arc environments (e.g. Reagan et al., 2010). Decompression-melting of subduction-modified (i.e. hybridized) mantle could have occurred in the present-day tectonic setting of the TLTF arc, given that this constitutes the widely proposed petrogenetic model for the lavas in this region (McInnes and Cameron, 1994; Stracke and Hegner, 1998; Kamenov et al., 2005, 2008). However, the low temperatures of equilibration of TUBAF peridotites are impossible to reconcile with a recent mantle lithosphere formation process, i.e. synchronous with the birth of the TLTF arc (≤3.6 Ma; Rytuba et al., 1993). Slow cooling of mantle lithosphere from ≥1200 °C to ~700 °C typically requires timescales that are an order of magnitude longer (~25–30 Myrs; Tollan et al., 2017). On the basis of the decompression trend to shallow depths in TUBAF peridotites, we therefore suggest that the concurrent residual SSZ signatures in these rocks formed through mantle hybridization-melting in a fore-arc environment during the Oligocene to Miocene subduction along the Manus-Kilinailau trench (Fig. 1; Johnson, 1979; Coleman and Kroenke, 1981).

7. CONCLUSIONS

We report petrological and major and trace element data for a new suite of spinel harzburgite xenoliths from the mantle lithosphere beneath TUBAF seamount in the fore-arc region of New Ireland (Papua New Guinea area). The main results of this study are as follows:

(i) All samples are fresh peridotites displaying coarse-grained protogranular texture, and sometimes high orthopyroxene (up to ~29 wt%) at low clinopyroxene (≤4 wt%) contents.
(ii) TUBAF peridotites define a Fe-Al correlation along the 25–30% melting isopleths from ~2 to <1 GPa, which is associated with the distinctive enrichment in silica and (TiO_2, Al_2O_3, Na_2O)-depletion of SSZ peridotites. This unique association strongly supports the partial melting origin of these 'residual SSZ signatures'. TUBAF seamount is only the fifth locality on Earth where a Fe-Al correlation in residual mantle peridotites is found, and the first in a SSZ environment.
(iii) Bulk-rock and mineral major element compositions of TUBAF peridotites are similar to those of other residual SSZ peridotites, as it is the case for the abundances of lithophile trace elements, which indicate 25–30% of nearly-pure fractional melt extraction (critical mass porosity <0.001%) in the presence of a fluxing agent enriched in highly incompatible elements.
(iv) We present the results of polybaric flux-melting models including minor element partitioning parameterizations, and involving variably pre-depleted and hybridized (i.e. silica-enriched) mantle sources. The residual SSZ signatures are best reproduced when pre-depleted mantle protoliths (by ≥10% melting of the primitive mantle) are hybridized by hydrous, silica-rich liquids, such as those derived by melting of eclogite or subducted sediments.
(v) Post-melting metasomatism (including fibrous orthopyroxene that are absent from the samples in this study) are unrelated to silica enrichment in TUBAF and other SSZ peridotites, and to the formation of the residual SSZ signatures in general. The new data are used to re-assess earlier interpretations of the origins of TUBAF peridotites, which we demonstrate have experienced their last melting event in a mantle wedge, as true for samples from the Izu-Bonin-Mariana, Kamchatka and West Bismarck arcs.
(vi) From the unique Fe-Al correlation in TUBAF peridotites and their low temperatures of equilibration, it appears that fractional hybridization-melting processes forming these rocks occurred in a fore-arc environment with shallow mantle decompression, likely during Miocene subduction along the Manus-Kilinailau trench.

Declaration of Competing Interest

The authors declare that they have no known competing financial interests or personal relationships that could have appeared to influence the work reported in this paper.

ACKNOWLEDGEMENTS

This work was funded by grants to R.J.A. and O.N. (DP120104240 and DE120100513) from the Australian Research Council and O.M. (200021_162666) from the Swiss National Science Foundation. A.B. has received funding from the European Union's Horizon 2020 research and innovation programme under the Marie Skłodowska-Curie grant agreement 844795. A.B. is grateful to M. Robyr for providing assistance during EPMA analyses at UNIL, and J.-W. Park and A. Ulyanov during LA-ICP-MS analyses, respectively at ANU and UNIL.

APPENDIX A. SUPPLEMENTARY DATA

Supplementary data to this article can be found online at https://doi.org/10.1016/j.gca.2020.11.001.

REFERENCES

Arai S. (1994) Characterization of spinel peridotites by olivine-spinel compositional relationships: Review and interpretation. *Chem. Geol.* **113**, 191–204.

Baker M. B. and Beckett J. R. (1999) The origin of abyssal peridotites: a reinterpretation of constraints based on primary bulk compositions. *Earth Planet. Sci. Lett.* **171**, 49–61.

Baker M. B. and Stolper E. M. (1994) Determining the composition of high-pressure mantle melts using diamond aggregates. *Geochim. Cosmochim. Acta* **58**, 2811–2827.

Ballhaus C., Berry R. F. and Green D. H. (1991) High pressure experimental calibration of the olivine orthopyroxene-spinel oxygen geobarometer: implications for the oxidation state of the upper mantle. *Contrib. Mineral. Petrol.* **107**, 27–40.

Behn M. D., Kelemen P. B., Hirth G., Hacker B. R. and Massonne H.-J. (2011) Diapirs as the source of the sediment signature in arc lavas. *Nat. Geosci.* **4**, 641–646.

Bénard A. and Ionov D. A. (2012) A new petrogenetic model for low-Ca boninites: Evidence from veined sub-arc xenoliths on melt-mantle interaction and melt fractionation. *Geochem. Geophys. Geosyst.*. https://doi.org/10.1029/2012GC004145.

Bénard A. and Ionov D. A. (2013) Melt- and fluid-rock interaction in supra-subduction lithospheric mantle: evidence from andesite-hosted veined peridotite xenoliths. *J. Petrol.* **54**, 2339–2378.

Bénard A., Nebel O., Ionov D. A., Arculus R. J., Shimizu N. and Métrich N. (2016) Primary silica-rich picrite and high-Ca boninite melt inclusions in pyroxenite veins from the Kamchatka sub-arc mantle. *J. Petrol.* **57**, 1955–1982.

Bénard A., Arculus R. J., Nebel O., Ionov D. A. and McAlpine S. R. B. (2017a) Silica-enriched mantle sources of picrite-boninite-andesite island arc magmas. *Geochim. Cosmochim. Acta* **199**, 287–303.

Bénard A., Koga K. T., Shimizu N., Kendrick M. A., Ionov D. A., Nebel O. and Arculus R. J. (2017b) Chlorine and fluorine partition coefficients and abundances in sub-arc mantle xenoliths (Kamchatka, Russia): Implications for melt generation and volatile recycling processes in subduction zones. *Geochim. Cosmochim. Acta* **199**, 324–350.

Bénard A., Klimm K., Woodland A. B., Arculus R. J., Wilke M., Botcharnikov R. E., Shimizu N., Nebel O., Rivard C. and Ionov D. A. (2018b) Oxidising agents in sub-arc mantle melts link slab devolatilisation and arc magmas. *Nat. Commun.*. https://doi.org/10.1038/s41467-018-05804-2.

Bénard A., Woodland A. B., Arculus R. J., Nebel O. and McAlpine S. R. B. (2018a) Variation in sub-arc mantle oxygen fugacity during partial melting recorded in refractory peridotite xenoliths from the West Bismarck Arc. *Chem. Geol.* **486**, 16–30.

Bird P. (2003) An updated digital model of plate boundaries. *Geochem. Geophys. Geosyst.*. https://doi.org/10.1029/2001GC000252.

Brey G. P. and Köhler T. (1990) Geothermobarometry in four phase lherzolites II. New thermobarometers, and practical assessment of existing thermobarometers. *J. Petrol.* **31**, 1353–1378.

Carpenter R. L., Edgar A. D. and Thibault Y. (2002) Origin of spongy textures in clinopyroxene and spinel from mantle xenoliths, Hessian Depression, Germany. *Miner. Petrol.* **74**, 149–162.

Carroll M. R. and Wyllie P. J. (1989) Experimental phase relations in the system tonalite-peridotite-H_2O at 15 kb; Implications for assimilation and differentiation processes near the crust-mantle boundary. *J. Petrol.* **30**, 1351–1382.

Coleman P. J. and Kroenke L. W. (1981) Subduction without volcanism in the Solomon Islands arc. *Geo-Mar. Lett.* **1**, 129–134.

Dick H. J. B. and Bullen T. (1984) Chromium spinel as a petrogenetic indicator in abyssal and alpine-type peridotites and spatially associated lavas. *Contrib. Mineral. Petrol.* **86**, 54–76.

Doucet L.-S., Ionov D. A., Golovin A. V. and Pokhilenko N. P. (2012) Depth, degrees and tectonic settings of mantle melting during craton formation: inferences from major and trace element compositions of spinel harzburgite xenoliths from the Udachnaya kimberlite, central Siberia. *Earth Planet. Sci. Lett.* **359–360**, 206–218.

Eiler J. M., Schiano P., Kitchen N. and Stolper E. M. (2000) Oxygen-isotope evidence for recycled crust in the sources of mid-ocean-ridge basalts. *Nature* **403**, 530–534.

Endo S., Mizukami T., Wallis S. R., Akihiro T. and Arai S. (2015) Orthopyroxene-rich rocks from the Sanbagawa Belt (SW Japan): Fluid-rock interaction in the forearc slab-mantle wedge interface. *J. Petrol.* **56**, 1113–1137.

Exon N. F., Stewart W. D., Sandy M. J. and Tiffin D. L. (1986) Geology and offshore petroleum prospects of the eastern New Ireland Basin, northeastern Papua New Guinea. *BMR J. Aust. Geol. Geophys.* **10**, 39–51.

Foden J., Sossi P. A. and Nebel O. (2018) Controls on the iron isotopic composition of global arc magmas. *Earth Planet Sci. Lett.* **494**, 190–201.

Franz L., Becker K.-P., Kramer W. and Herzig P. M. (2002) Metasomatic mantle xenoliths from the Bismarck Microplate (Papua New Guinea)—thermal evolution, geochemistry and extent of slab-induced metasomatism. *J. Petrol.* **43**, 315–343.

Franz L. and Romer R. L. (2010) Different style of metasomatic veining in ultramafic xenoliths from the TUBAF Seamount (Bismarck Microplate, Papua New Guinea). *Lithos* **114**, 30–53.

Gaetani G. A. and Grove T. L. (1998) The influence of water on melting of mantle peridotite. *Contrib. Mineral. Petrol.* **131**, 326–346.

Gao S., Liu X., Yuan H., Hattendorf B., Günther D., Chen L. and Hu S. (2002) Determination of forty two major and trace elements in USGS and NIST SRM glasses by laser ablation-inductively coupled plasma-mass spectrometry. *Geostand. News.* **26**, 181–196.

Ghiorso M. S., Hirschmann M. M., Reiners P. W. and Kress, III, V. C. (2002) The pMELTS: a revision of MELTS for improved calculation of phase relations and major element partitioning related to partial melting of the mantle to 3 GPa. *Geochem. Geophys. Geosyst.*. https://doi.org/10.1029/2001GC000217.

Grégoire M., McInnes B. I. A. and O'Reilly S. Y. (2001) Hydrous metasomatism of oceanic sub-arc mantle, Lihir, Papua New Guinea: Part 2. Trace element characteristics of slab-derived fluids. *Lithos* **59**, 91–108.

Hellebrand E., Snow J. E., Dick H. J. B. and Hofmann A. W. (2001) Coupled major and trace elements as indicators of the extent of melting in mid-ocean-ridge peridotites. *Nature* **410**, 677–681.

Hermann J. and Spandler C. J. (2008) Sediment melts at sub-arc depths: an experimental study. *J. Petrol.* **49**, 717–740.

Herzberg C. (2004) Geodynamic information in peridotite petrology. *J. Petrol.* **45**, 2507–2530.

Hirose K. and Kawamoto T. (1995) Hydrous partial melting of lherzolite at 1 GPa: The effect of H_2O on the genesis of basaltic magmas. *Earth Planet Sci. Lett.* **133**, 463–473.

Ionov D. A. (2004) Chemical variations in peridotite xenoliths from Vitim, Siberia: Inferences for REE and Hf behaviour in the garnet-facies upper mantle. *J. Petrol.* **45**, 343–367.

Ionov D. A. (2007) Compositional variations and heterogeneity in fertile lithospheric mantle: peridotite xenoliths in basalts from Tariat, Mongolia. *Contrib. Mineral. Petrol.* **154**, 455–477.

Ionov D. A. (2010) Petrology of mantle wedge lithosphere: New data on supra-subduction zone peridotite xenoliths from the andesitic Avacha volcano, Kamchatka. *J. Petrol.* **51**, 327–361.

Ionov D. A., Bodinier J.-L., Mukasa S. B. and Zanetti A. (2002) Mechanisms and sources of mantle metasomatism: major and trace element compositions of peridotite xenoliths from Spitsbergen in the context of numerical modeling. *J. Petrol.* **43**, 2219–2259.

Ionov D. A., Chanefo I. and Bodinier J.-L. (2005) Origin of Fe-rich lherzolites and wehrlites from Tok, SE Siberia by reactive melt percolation in refractory mantle peridotites. *Contrib. Mineral. Petrol.* **150**, 335–353.

Ionov D. A., Bénard A. and Plechov P. Y. (2011) Melt evolution in subarc mantle: evidence from heating experiments on spinel-hosted melt inclusions in peridotite xenoliths from the andesitic Avacha volcano (Kamchatka, Russia). *Contrib. Mineral. Petrol.* **162**, 1159–1174.

Ionov D. A., Bénard A., Plechov P. Y. and Shcherbakov V. D. (2013) Along-arc variations in lithospheric mantle compositions in Kamchatka, Russia: first trace element data on mantle xenoliths from the Klyuchevskoy group volcanoes. *J. Volcanol. Geotherm. Res.* **263**, 122–131.

Ionov D. A. and Hofmann A. W. (2007) Depth of formation of subcontinental off-craton peridotites. *Earth Planet. Sci. Lett.* **261**, 620–634.

Inoue T. (1994) Effect of water on melting phase relations and melt composition in the system Mg_2SiO_4–$MgSiO_3$–H_2O up to 15 GPa. *Phys. Earth Planet Int.* **85**, 237–263.

Ishimaru S., Arai S., Ishida Y., Shirasaka M. and Okrugin V. M. (2007) Melting and multi-stage metasomatism in the mantle wedge beneath a frontal arc inferred from highly depleted peridotite xenoliths from the Avacha volcano, southern Kamchatka. *J. Petrol.* **48**, 395–433.

Jochum K. P., Willbold M., Raczek I., Stoll B. and Herwing K. (2005) Chemical characterisation of the USGS reference glasses GSA-1G, GSC-1G, GSD-1G, GSE-1G, BCR-2G, BHVO-2G and BIR-1G using EPMA, ID-TIMS, ID-ICP-MS and LA-ICP-MS. *Geostand. Geoanal. Res.* **29**, 285–302.

Jochum K. P., Weis U., Stoll B., Kuzmin D., Yang Q., Raczek I., Jacob D. E., Stracke A., Birbaum K., Frick D. A., Günther D. and Enzweiler J. (2011) Determination of reference values for NIST SRM 610–617 glasses following ISO guidelines. *Geostand. Geoanal. Res.* **35**, 397–429.

Johnson R. W. (1979) Geotectonics and volcanism in Papua New Guinea: a review of the late Cenozoic. *BMR J. Aust. Geol. Geophys.* **4**, 181–207.

Johnson R. W., Wallace D. A. and Ellis D. J. (1976) Feldspathoid-bearing potassic rocks and associated types from volcanic islands off the coast of New Ireland, Papua New Guinea: a preliminary account of geology and petrology. In *Volcanism in Australasia* (ed. R. W. Johnson). Elsevier Ltd., Amsterdam, pp. 297–316.

Johnston A. D. and Wyllie P. J. (1989) The system tonalite-peridotite-H_2O at 30 kbar, with applications to hybridization in subduction zone magmatism. *Contrib. Mineral. Petrol.* **102**, 257–264.

Kamenov G. D., Perfit M. R., Jonasson I. R. and Mueller P. A. (2005) High-precision Pb isotope measurements reveal magma recharge for ore deposit formation: Examples from Lihir Island and Conical seamount, Papua New Guinea. *Chem. Geol.* **219**, 131–148.

Kamenov G. D., Perfit M. R., Mueller P. A. and Jonasson I. R. (2008) Controls on magmatism in an island arc environment: study of lavas and sub-arc xenoliths from the Tabar-Lihir-Tanga-Feni island chain, Papua New Guinea. *Contrib. Mineral. Petrol.* **155**, 635–656.

Kennedy A. K., Grove T. L. and Johnson R. W. (1990) Experimental and major element constraints on the evolution of lavas from Lihir Island, Papua New Guinea. *Contrib. Mineral. Petrol.* **104**, 722–734.

Kessel R., Schmidt M. W., Ulmer P. and Pettke T. (2005) Trace element signature of subduction-zone fluids, melts and supercritical liquids at 120–180 km depth. *Nature* **437**, 724–727.

Kimura (2017) Modeling chemical geodynamics of subduction zones using the Arc Basalt Simulator version 5. *Geosphere*. https://doi.org/10.1130/GES01468.1.

Kinzler R. J. (1997) Melting of mantle peridotite at pressures approaching the spinel to garnet transition: Application to mid-ocean ridge basalt petrogenesis. *J. Geophys. Res.* **102**, 853–874.

Kinzler R. J. and Grove T. L. (1992) Primary magmas of mid-ocean ridge basalts 1. Experiments and methods. *J. Geophys. Res.* **97**, 6885–6906.

Kushiro I., Yoder, Jr, H. S. and Nishikawa M. (1968) Effect of water on the melting of enstatite. *Geol. Soc. Am. bull.* **79**, 1685–1692.

Lindley I. D. (2016) Plate flexure and volcanism: Late Cenozoic tectonics of the Tabar-Lihir-Tanga-Feni alkalic province, New Ireland Basin, Papua New Guinea. *Tectonophysics* **677–678**, 312–323.

Mallik A., Nelson J. and Dasgupta R. (2015) Partial melting of fertile peridotite fluxed by hydrous rhyolitic melt at 2–3 GPa: implications for mantle wedge hybridization by sediment melt and generation of ultrapotassic magmas in convergent margins. *Contrib. Mineral. Petrol.* **169**, 48.

Mallik A., Dasgupta R., Tsuno K. and Nelson J. (2016) Effects of water, depth and temperature on partial melting of mantle-wedge fluxed by hydrous sediment-melt in subduction zones. *Geochim. Cosmochim. Acta* **195**, 226–243.

Malvoisin B. (2015) Mass transfer in the oceanic lithosphere: Serpentinization is not isochemical. *Earth Planet. Sci. Lett.* **430**, 75–85.

Manning C. E. (2004) The chemistry of subduction-zone fluids. *Earth Planet. Sci. Lett.* **223**, 1–16.

Maury R. C., Defant M. J. and Joron J. L. (1992) Metasomatism of the sub-arc mantle inferred from trace elements in Philippine xenoliths. *Nature* **360**, 661–663.

McDade P., Blundy J. D. and Wood B. J. (2003a) Trace element partitioning on the Tinaquillo Lherzolite solidus at 1.5 GPa. *Phys. Earth Planet Int.* **139**, 129–147.

McDade P., Blundy J. D. and Wood B. J. (2003b) Trace element partitioning between mantle wedge peridotite and hydrous MgO-rich melt. *Am. Min.* **88**, 1825–1831.

McDonough W. F. and Sun S.-S. (1995) The composition of the Earth. *Chem. Geol.* **120**, 223–253.

McInnes B. I. A. and Cameron E. M. (1994) Carbonated, alkaline hybridizing melts from a sub-arc environment: Mantle wedge samples from the Tabar-Lihir-Tanga-Feni arc, Papua New Guinea. *Earth Planet. Sci. Lett.* **122**, 125–141.

McInnes B. I. A., Gregoire M., Binns R. A., Herzig P. M. and Hannington M. D. (2001) Hydrous metasomatism of oceanic sub-arc mantle, Lihir, Papua New Guinea: petrology and geochemistry of fluid-metasomatised mantle wedge xenoliths. *Earth Planet. Sci. Lett.* **188**, 169–183.

Müntener O. and Manatschal G. (2006) High degrees of melt extraction recorded by spinel harzburgite of the Newfoundland margin: The role of inheritance and consequences for the evolution of the southern North Atlantic. *Earth Planet. Sci. Lett.* **252**, 437–452.

Nebel O., Sossi P. A., Bénard A., Wille M., Vroon P. Z. and Arculus R. J. (2015) Redox-variability and controls in subduction zones from an iron-isotope perspective. *Earth Planet. Sci. Lett.* **432**, 142–151.

Nebel O., Sossi P. A., Foden J., Bénard A., Brandl P. A., Stammeier J. A., Lupton J., Richter M. and Arculus R. J. (2018) Iron isotope variability in ocean floor lavas and mantle sources in the Lau back-arc basin. *Geochim. Cosmochim. Acta* **241**, 150–163.

Niu Y. and Hékinian R. (1997) Basaltic liquids and harzburgitic residues in the Garrett transform: a case study at fast-spreading ridges. *Earth Planet. Sci. Lett.* **146**, 243–258.

O'Neill H. St. C. and Wall V. J. (1987) The olivine–orthopyroxene–spinel oxygen geobarometer, the nickel precipitation curve, and the oxygen fugacity of the Earth's upper mantle. *J. Petrol.* **28**, 1169–1191.

Pagé P., Bédard J. H. and Tremblay A. (2009) Geochemical variations in a depleted fore-arc mantle: The Ordovician Thetford Mines Ophiolite. *Lithos* **113**, 21–47.

Palme H. and O'Neill H. St. C. (2014) Cosmochemical estimates of mantle composition. In *Treatise on Geochemistry* (eds. K. Turekian and H. Holland), 2nd edition. Elsevier Ltd., Amsterdam, pp. 1–39.

Pan S., Zheng J., Yin Z., Griffin W. L., Xia M., Lin A. and Zhang H. (2018) Spongy texture in mantle clinopyroxene records decompression-induced melting. *Lithos* **320–321**, 144–154.

Parkinson I. J. and Pearce J. A. (1998) Peridotites from the Izu-Bonin-Mariana forearc (ODP leg 125): Evidence for mantle melting and melt-mantle interaction in a supra-subduction zone setting. *J. Petrol.* **39**, 1577–1618.

Parman S. W. and Grove T. L. (2004) Harzburgite melting with and without H_2O: experimental data and predictive modeling. *J. Geophys. Res.*. https://doi.org/10.1029/2003JB002566.

Pearce J. A., Barker P. F., Edwards S. J., Parkinson I. J. and Leat P. T. (2000) Geochemistry and tectonic significance of peridotites from the South Sandwich arc-basin system, South Atlantic. *Contrib. Mineral. Petrol.* **139**, 36–53.

Rapp R. P., Shimizu N., Norman M. D. and Applegate G. S. (1999) Reaction between slab-derived melts and peridotite in the mantle wedge: experimental constraints at 3.8 GPa. *Chem. Geol.* **160**, 335–356.

Rapp R. P., Norman M. D., Laporte D., Yaxley G. M., Martin H. and Foley S. F. (2010) Continent formation in the Archean and chemical evolution of the cratonic lithosphere: Melt-rock reaction experiments at 3–4 GPa and petrogenesis of Archean Mg-diorites (sanukitoids). *J. Petrol.* **51**, 1237–1266.

Reagan M. K., Ishizuka O., Stern R. J., Kelley K. A., Blichert-Toft J., Bloomer S. H., Cash J., Fryer P., Hanan B. B., Hickey-Vargas R., Ishii T., Kimura J.-I., Peate D. W., Rowe M. C. and Woods M. (2010) Fore-arc basalts and subduction initiation in the Izu-Bonin-Mariana system. *Geochem. Geophys. Geosyst.*. https://doi.org/10.1029/2009GC002871.

Rytuba J. J., McKee E. H. and Cox D. P. (1993) Geochronology and geochemistry of the Ladolam gold deposit, Lihir Island, and gold deposits and volcanoes of Tabar and Tatau, Papua New Guinea. *U.S Geol. Surv. Bull.* **2039**, 119–126.

Salters V. J. M. and Stracke A. (2004) Composition of the depleted mantle. *Geochem. Geophys. Geosyst.*. https://doi.org/10.1029/2003GC000597.

Sekine T. and Wyllie P. J. (1982) The system granite-peridotite-H_2O at 30 kbar, with applications to hybridization in subduction zone magmatism. *Contrib. Mineral. Petrol.* **81**, 190–202.

Shannon R. D. (1976) Revised effective ionic radii and systematic studies of interatomic distances in halides and chalcogenides. *Acta Cryst.* **A32**, 751–767.

Shaw D. (1970) Trace element fractionation during anatexis. *Geochim. Cosmochim. Acta* **34**, 237–243.

Shaw C. S. J. (2009) Textural development of amphibole during breakdown reactions in a synthetic peridotite. *Lithos* **110**, 215–228.

Shaw C. S. J. and Dingwell D. B. (2008) Experimental peridotite-melt reaction at one atmosphere: a textural and chemical study. *Contrib. Mineral. Petrol.* **155**, 199–214.

Shaw C. S. J., Heildelbach F. and Dingwell D. B. (2006) The origin of reaction textures in mantle peridotite xenoliths from Sal Island, Cape Verde: the case for "metasomatism" by the host lava. *Contrib. Mineral. Petrol.* **151**, 681–697.

Shaw C. S. J. and Klügel A. (2002) The pressure and temperature conditions and timing of glass formation in mantle-derived xenoliths from Baarley, West Eifel, Germany: the case for amphibole breakdown, lava infiltration and mineral-melt interaction. *Miner. Petrol.* **74**, 163–187.

Shea T. and Hammer J. E. (2013) Kinetics of cooling- and decompression-induced crystallization in hydrous mafic-intermediate magmas. *J. Volcanol. Geotherm. Res.* **260**, 127–145.

Soustelle V., Tommasi A., Demouchy S. and Ionov D. A. (2010) Deformation and fluid-rock interaction in the supra-subduction mantle: Microstructures and water contents in peridotite xenoliths from the Avacha volcano, Kamchatka. *J. Petrol.* **51**, 363–394.

Soustelle V., Tommasi A., Demouchy S. and Franz L. (2013) Melt-rock interactions, deformation, hydration and seismic properties in the sub-arc lithospheric mantle inferred from xenoliths from seamounts near Lihir, Papua New Guinea. *Tectonophysics* **608**, 330–345.

Stephens C. J. (1997) Heterogeneity of oceanic peridotite from the Western Canyon Wall at Mark: Results from site 920. In *Proc. ODP, Sci. Results*, vol. 153 (eds. J. A. Karson, M. Cannat, D. J. Miller and D. Elthon). College Station, TX (Ocean Drilling Program), pp. 285–303.

Stolper E. and Newman S. (1994) The role of water in the petrogenesis of Mariana trough magmas. *Earth Planet. Sci. Lett.* **121**, 293–325.

Stracke A. and Hegner E. (1998) Rifting-related volcanism in an oceanic post-collisional setting: the Tabar-Lihir Tanga-Feni (TLTF) island chain, Papua New Guinea. *Lithos* **45**, 545–560.

Syracuse E. M., van Keken P. E. and Abers G. A. (2010) The global range of suduction zone thermal models. *Phys. Earth Planet. Inter.* **183**, 73–90.

Takazawa E., Frey F., Shimizu N. and Obata M. (1996) Evolution of the Horoman Peridotite (Hokkaido, Japan): Implications from pyroxene compositions. *Chem. Geol.* **134**, 3–26.

Takazawa E., Frey F. A., Shimizu N. and Obata M. (2000) Whole rock compositional variations in an upper mantle peridotite (Horoman, Hokkaido, Japan): are they consistent with a partial melting process. *Geochim. Cosmochim. Acta* **64**, 695–716.

Taylor B. (1979) Bismarck Sea: evolution of a back-arc basin. *Geology* **7**, 171–174.

Tollan P. M. E., Dale C. W., Hermann J., Davidson J. P. and Arculus R. J. (2017) Generation and modification of the mantle wedge and lithosphere beneath the West Bismarck island arc: Melting, metasomatism and thermal history of peridotite xenoliths from Ritter island. *J. Petrol.* **58**, 1475–1510.

Voigt M. and von der Handt A. (2011) Influence of sub-solidus processes on the chromium number in spinel in ultramafic rocks. *Contrib. Mineral. Petrol.* **162**, 675–689.

Walter M. J. (1998) Melting of garnet peridotite and the origin of komatiite and depleted lithosphere. *J. Petrol.* **39**, 29–60.

Walter M. J. and Presnall D. C. (1994) Melting behavior of simplified lherzolite in the system $CaO–MgO–Al_2O_3–SiO_2–Na_2O$ from 7 to 35 kbar. *J. Petrol.* **35**, 329–359.

Walter M. J., Sisson T. W. and Presnall D. C. (1995) A mass proportion method for calculating melting reactions and application to melting of model upper mantle lherzolite. *Earth Planet. Sci. Lett.* **135**, 77–90.

Wang Z. and Gaetani G. A. (2008) Partitioning of Ni between olivine and siliceous eclogite partial melt: experimental constraints on the mantle source of Hawaiian basalts. *Contrib. Mineral. Petrol.* **156**, 661–678.

Warren J. M. (2016) Global variations in abyssal peridotite compositions. *Lithos* **87**, 193–219.

Weissel J. K., Taylor B. and Karner G. D. (1982) The opening of the Woodlark Basin, subduction of the Woodlark spreading system and the evolution of northern Melanesia since mid-Pliocene time. *Tectonophysics* **87**, 253–277.

Witt-Eickschen G. and O'Neill H. St. C. (2005) The effect of temperature on the equilibrium distribution of trace elements between clinopyroxene, orthopyroxene, olivine and spinel in upper mantle peridotite. *Chem. Geol.* **221**, 65–101.

Wittig N., Pearson D. G., Webb M., Ottley C. J., Irvine G. J., Kopylova M., Jensen S. M. and Nowell G. M. (2008) Origin of cratonic lithospheric mantle roots: a geochemical study of peridotites from the North Atlantic Craton, West Greenland. *Earth Planet. Sci. Lett.* **274**, 24–33.

Wood B. J., Taras Bryndzia L. and Johnson K. E. (1990) Mantle oxidation state and its relationship to tectonic environment and fluid speciation. *Science* **248**, 337–345.

Woodhead J., Eggins S. and Gamble J. (1993) High field strength and transition element systematics in island arc and back-arc basin basalts: evidence for multi-phase melt extraction and a depleted mantle wedge. *Earth Planet. Sci. Lett.* **114**, 491–504.

Woodland A. B., Bulatov V. K., Brey G. P., Girnis A. V., Höfer H. E. and Gerdes A. (2018) Subduction factory in an ampoule: Experiments on sediment-peridotite interaction under temperature gradient conditions. *Geochim. Cosmochim. Acta* **223**, 319–349.

Workman R. K. and Hart S. R. (2005) Major and trace element composition of the depleted MORB mantle (DMM). *Earth Planet. Sci. Lett.* **231**, 53–72.

Yaxley G. M. and Green D. H. (1998) Reactions between eclogite and peridotite: mantle refertilisation by subduction of oceanic crust. *Schweiz. Mineral. Petrogr. Mitt.* **78**, 243–255.

Zou H. (1998) Trace element fractionation during modal and nonmodal dynamic melting and open-system melting: A mathematical treatment. *Geochim. Cosmochim. Acta* **62**, 1937–1945.

Associate editor: Bernard Charlier